New Insights on Subsurface Geology and the San Andreas Fault at Loma Prieta, Central California

Gary S. Fuis^{*1}, Rufus D. Catchings¹, Daniel S. Scheirer¹, Klaus Bauer², Mark Goldman¹, Tait E. Earney¹ Guoqing Lin³, and Edward Zhang^{1,4}

ABSTRACT

The 1989 M_w 6.9 Loma Prieta earthquake is the first major event to occur along the San Andreas fault (SAF) zone in central California since the 1906 M 7.9 San Francisco earthquake. Given the complexity of this event, uncertainty has persisted as to whether this earthquake ruptured the SAF itself or a secondary fault. Recent work on the SAF in the Coachella Valley in southern California has revealed similar complexity, arising from a nonplanar, nonvertical fault geometry, and has led us to reexamine the Loma Prieta event. We have compiled data sets and data analyses in the vicinity of the Loma Prieta earthquake, including the 3D seismic velocity model and aftershock relocations of Lin and Thurber (2012), potential field data collected by the U.S. Geological Survey following the earthquake, and seismic refraction and reflection data from the 1991 profile of Catchings et al. (2004). The velocity model and aftershock relocations of Lin and Thurber (2012) reveal a geometry for the SAF that appears similar to that in the Coachella Valley (although rotated 180°): at Loma Prieta the fault dips steeply near the surface and curves with depth to join the moderately southwest-dipping main rupture below 6 km depth, itself also nonplanar. The SAF is a clear velocity boundary, with higher velocities on the northeast, attributable to Mesozoic accretionary and other rocks, and lower velocities on the southwest, attributable to Cenozoic sedimentary and volcanic rocks of the La Honda block. Rocks of the La Honda block have been offset right-laterally hundreds of kilometers from similar rocks in the southern San Joaquin Valley and vicinity, providing evidence that the curved northeast fault boundary of this block is the plate boundary. Thus, we interpret that the Loma Prieta earthquake occurred on the SAF and not on a secondary fault.

KEY POINTS

- Did the 1989 Loma Prieta earthquake occur on the San Andreas fault, and what is the fault geometry?
- The earthquake occurred on the San Andreas fault, and the fault is both nonvertical and nonplanar.
- This San Andreas fault geometry is not unique to Loma Prieta.

Supplemental Material

INTRODUCTION

Loma Prieta, in central California, was the site of an $M_{\rm w}$ 6.9 earthquake in 1989, which was the first major event to occur along the San Andreas fault (SAF) zone in this region since the 1906 M 7.9 San Francisco earthquake. The earthquake was complex, with a mainshock rupture on a moderately southwest-dipping surface that terminated upward at about 6 km depth (Beroza, 1991, 1996; Wald et al., 1991; Dietz and Ellsworth, 1997). Above 6 km depth, the majority of aftershocks actually plot northeast of the surface trace of the SAF, in some cases

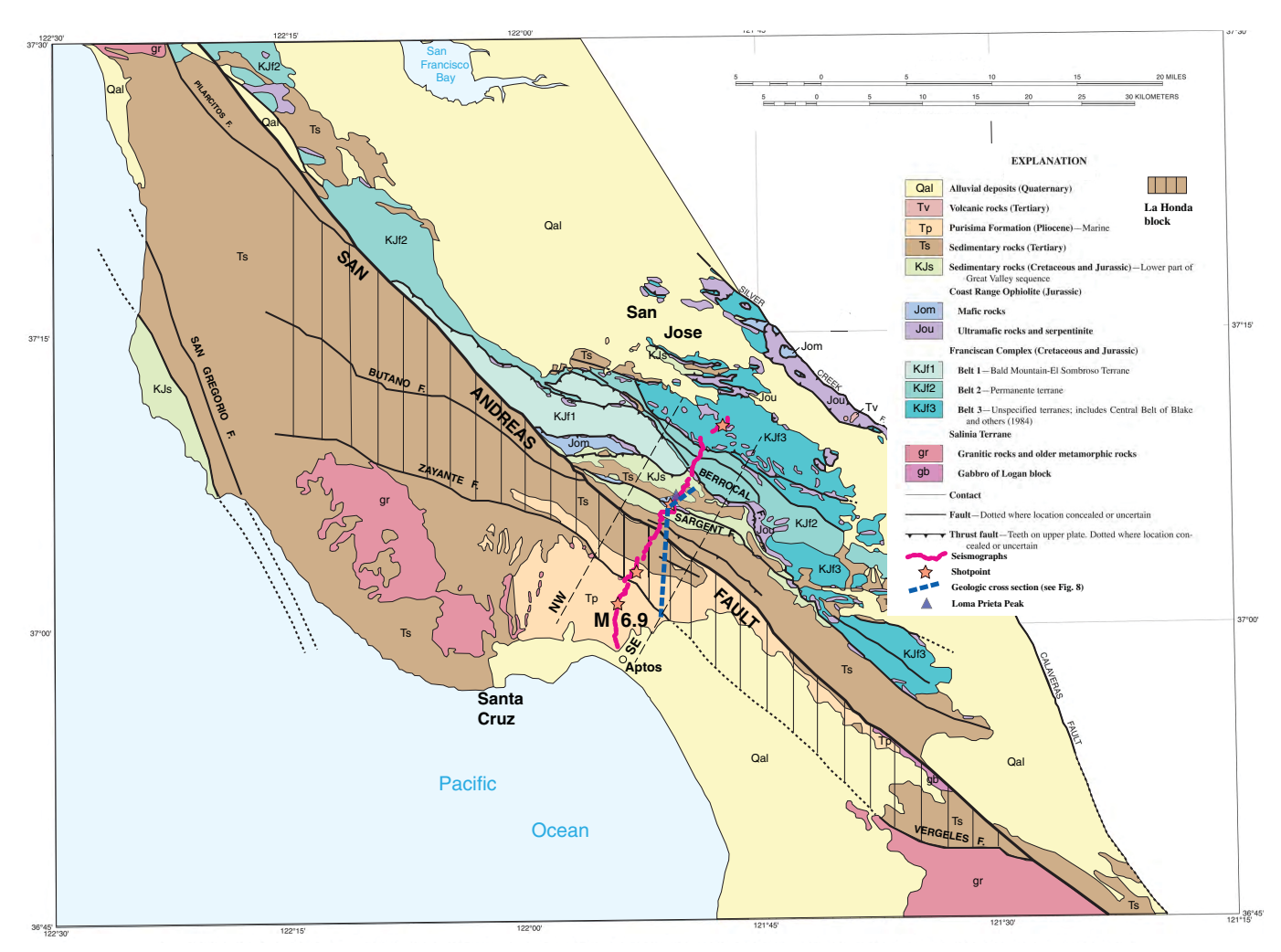
giving the impression that the surface projection of the rupture might be the Sargent fault (see Fig. 1 for location)—a strike-slip fault within the SAF zone (see Dietz and Ellsworth, 1997, their figs. 20H, 20K). There is little evidence of a vertical SAF, although there are a couple of steeply dipping clusters of aftershocks in aftershock cross sections (e.g., Dietz and Ellsworth, 1997, their fig. 22D2). Nevertheless, a vertical, largely aseismic SAF is featured as a possible, although not necessarily preferred, interpretation in many publications, including those of Dietz

1. U.S. Geological Survey, Menlo Park, California, U.S.A., b https://orcid.org/0000-0002-3078-1544 (GSF); https://orcid.org/0000-0002-5191-6102 (RDC); https:// (MG); (b) https://orcid.org/0000-0002-1504-0457 (TEE); (b) https://orcid.org/0000-0003-4923-8733 (EZ); 2. Deutsches GeoForschungsZentrum (GFZ), Potsdam, Germany; 3. Department of Marine Geosciences, Rosenstiel School of Marine, Atmospheric, and Earth Science, University of Miami, Miami, Florida, U.S.A., https://orcid.org/0000-0003-2858-7782 (GL); 4. Systems & Technology Research, Woburn, Massachusetts, U.S.A.

*Corresponding author: fuis@usgs.gov

Cite this article as Fuis, G. S., R. D. Catchings, D. S. Scheirer, K. Bauer, M. Goldman, T. E. Earney, G. Lin, and E. Zhang (2022). New Insights on Subsurface Geology and the San Andreas Fault at Loma Prieta, Central California, Bull. Seismol. Soc. Am. XX, 1-20, doi: 10.1785/0120220037

© Seismological Society of America



Generalized geologic map of Loma Prieta area

and Ellsworth (1990, their fig. 5; 1997 [text]) and Eberhart-Phillips and Michael (1998, their plate 2; 2004, their fig. 6). The possibilities that a vertical SAF offsets a dipping rupture represented by the Loma Prieta aftershock zone, or vice versa, were allowed, although one interpretation by Dietz and Ellsworth (1990), namely that the SAF itself bent upward at about 9 km depth to intersect its surface trace, is not dissimilar to the interpretation in this study. The question remained: Was the Loma Prieta earthquake on the SAF or a secondary fault.

Further complexity for the Loma Prieta earthquake arises from the oblique slip northwest of the epicenter and the simpler strike slip southeast of the epicenter (Beroza, 1996). Aftershock patterns are complex northwest of the epicenter, similar to that described earlier, with the aftershock zone generally projecting northeast of the surface trace; however, aftershock patterns southeast of the epicenter are simpler and tend to project to the surface trace of the SAF (Dietz and Ellsworth, 1997). These latter authors point out that this transition in slip is located where the SAF steps to the left by a few kilometers and may be caused by the slip of material around a compressional bend (Dietz and Ellsworth, 1997, their fig. 27).

Figure 1. Generalized geologic map of Loma Prieta area after McLaughlin and Griscom (2004, pl. 3). Focal mechanism plot, Northern California Seismic Network (NCSN) focal mechanism of mainshock plotted at 3D relocation; M 6.9, magnitude of Loma Prieta earthquake. For all other symbols, see explanation inside figure, including red line, active-source receivers; orange stars, shot points; NW, SE, additional lines along which seismicity and seismic velocities are plotted in this study; blue dashed line, location of geologic cross section; and vertical-lined pattern, La Honda block. NW, northwest; SE, southeast.

Most research on the Loma Prieta earthquake occurred in the 1990s and early 2000s. During and after that time new analysis methods have been developed, including double-difference and waveform cross-correlation methods (Waldhauser and Ellsworth, 2000) that allowed aftershock clusters to be more sharply imaged, and also 3D arrival-time inversion (e.g., Foxall *et al.*, 1993; Eberhart-Phillips and Michael, 1998, 2004; Thurber *et al.*, 2007) that allowed 3D velocity models to supercede 1D models. Increases in computer power allowed these new methods to be applied to massive data sets (e.g., Hauksson and Shearer, 2005; Schaff and Waldhauser,

2005; Lin, Shearer, and Hauksson, 2007; Waldhauser and Schaff, 2008). This advance was followed by development of the composite event approach (Lin, Shearer, and Hauksson, 2007; Lin et al., 2007; Lin and Thurber, 2012) that permitted more uniform event distribution in earthquake analysis along with increased accuracy in and numbers of arrival times for both P and S waves. Accompanying this improvement in earthquake analysis, active-source imaging was applied in a number of locations in both central California (Catchings et al., 2004) and southern California (e.g., Fuis et al., 2001, 2003, 2017), allowing, through increases in numbers of sources and receivers, much higher and deeper resolution of crustal velocity structure. Along with fielding active-source experiments, came the development of a method for detecting and migrating low-fold reflections present in the codas of explosions (Bauer et al., 2013). Finally, advances in software for analyzing potential field data has allowed rapid testing of numerous models (see what follows and supplemental material available to this article).

The application of the advances described earlier to data collected in the active-source Salton Seismic Imaging Project allowed Fuis et al. (2017) to resolve a nonvertical and nonplanar SAF in two locations in the Coachella Valley of southern California. In these locations, the SAF is steep in the upper 6-9 km but dips moderately northeast below that depth. In one location, aftershocks of the 1986 $M_{\rm w}$ 6.1 North Palm Springs earthquake do not clearly project upward to the surface traces of the SAF (Banning and Garnet Hill faults) but appear to project to the south or southwest of those traces. Similarly, at the second location, seismicity along the northeast-dipping segment of the (creeping) SAF does not project upward to the trace of the SAF but to the southwest of the trace. These images of the SAF are obtained from analysis of earthquakes, using double-difference, waveform cross correlation and cluster analysis (Hauksson et al., 2012), detection and migration of steep reflections in the coda of explosions, using the method of Bauer et al. (2013), and analysis of both gravity and aeromagnetic data.

In this current study of the SAF at Loma Prieta, we use the same data analysis techniques as in the Coachella Valley. For earthquake analysis, we use the existing results of Lin and Thurber (2012). We combine their velocity model with our own along our active-source profile, which is similar to the velocity model of Catchings et al. (2004). We analyze reflections in the active-source coda using the method of Bauer et al. (2013). Finally, we model potential field data along our activesource profile, using as guides prior modeling by Jachens and Griscom (2004) along a parallel profile 5 km southeast of our profile and also a geologic cross section by McLaughlin et al. (2004) very close to our profile.

The fault geometry we infer in this study at Loma Prieta appears similar to that imaged in the Coachella Valley, although the SAF dips in opposite directions in these two locations. Thus, at Loma Prieta, we interpret that the SAF is nonvertical and nonplanar. As this study will show, the SAF forms a clear, curving velocity boundary between Mesozoic accretionary and other rocks on its northeast side and Cenozoic sedimentary and volcanic rocks on its southwest side. The Cenozoic sedimentary and volcanic rocks constitute the La Honda block, as discussed subsequently, and the other half of this block is offset hundreds of kilometers right laterally to the southern San Joaquin Valley and vicinity. We thus interpret that the fault that ruptured at Loma Prieta in 1989 is, in fact, the SAF and not the secondary fault shown in prior interpretations.

GEOLOGIC SETTING

In the Coast Ranges of central California, geology differs significantly between the Pacific and North American plates, on either side of the plate-bounding SAF zone (Fig. 1). The Pacific plate is composed of a sequence of clastic sedimentary rocks and minor volcanic rocks deposited, where it can be determined by exposure and oil-well data, on a basement of Salinian granitic and metamorphic rocks. The basement is described by Ross (1970, 1978). Northeast of the San Gregorio fault, an active Neogene strike-slip fault located near the coast, the sedimentary and volcanic sequence is described by Cummings et al. (1962), Clark (1981), Stanley (1985), and McLaughlin and Clark (2004). This sequence contains rocks from every epoch of the Cenozoic deposited in a basin in offshore California known as the La Honda basin. Rocks southwest of the San Gregorio fault were deposited in a basin farther south.

The North American plate consists of Mesozoic accretionary rocks, the California Great Valley Sequence, and Tertiary sedimentary rocks. The Mesozoic accretionary rocks include the Franciscan Complex and ophiolitic rocks. These rocks are summarized by McLaughlin and Clark (2004) and McLaughlin et al. (2004).

Rocks of the Pacific plate in the Coast Ranges are divided into three blocks by the San Gregorio and Zayante-Vergeles faults (Fig. 1). The Zayante-Vergeles fault (or Zayante fault) is an inactive Cenozoic reverse fault. Rocks southwest of the San Gregorio fault include Mesozoic clastic sedimentary and volcanic rocks, and basement is not exposed in the Coast Ranges. The rocks between the San Gregorio and Zayante faults constitute the Ben Lomond block and consist of thin (<3 km) Cenozoic sedimentary and volcanic rocks over Salinian granitic and metamorphic basement. The rocks between the Zayante fault and SAF constitute a 10 km thick sequence (this study) known as the La Honda block (Fig. 1). Basement is not exposed except in the northern part of the San Francisco peninsula, where it is granitic (Fig. 1). However, farther south, basement may include ophiolitic rocks of which the Logan gabbro may be a fragment. It has a Jurassic age (James et al., 1994) and is exposed on the northeast side of the La Honda block at its southeastern end (see Fig. 1).

The other half of the La Honda block, on the northeast side of the SAF, is found in the southern San Joaquin Valley and mountains on its southwest and south sides. Some geologic formation names are even the same in this region (Stanley, 1985), and an outcrop of gabbro, the Eagle Rest Peak gabbro in the San Emigdio Mountains, has been correlated to the Logan gabbro (Ross, 1970). An extensive discussion of the links between the La Honda and San Joaquin basins can be found in Stanley (1985) and references therein and more recently in Gooley *et al.* (2020).

Rocks northeast of the SAF include the Franciscan Complex, ophiolitic rocks, sedimentary rocks of the California Great Valley Sequence, and Tertiary sedimentary rocks. These rocks are offset by numerous compressional and extensional faults; the Coast Range fault is a prominent extensional fault in this region. In addition, the Sargent fault is an important active strike-slip fault of the SAF system within these rocks (Fig. 1).

Asymmetry in rock types across the SAF zone is accompanied by asymmetry in deformation. Rocks of the Pacific plate are deformed chiefly by broad, open folds and a few steep faults, including the Zayante and Butano (dip-slip) faults (Fig. 1), that were active into the Pliocene but do not appear to be active in the Quaternary (McLaughlin and Clark, 2004). The Butano fault, like the Zayante fault, appears to be a reverse fault. On the North American plate, on the other hand, rocks are offset by numerous faults, including young reverse faults, such as the Berrocal and other faults in the Foothills fault zone along the northeast side of the San Francisco peninsula (McLaughlin, 1974; Aydin and Page, 1984). These latter faults appear to be secondary or flower-structure-like faults within the SAF system (Jachens and Griscom, 2004; McLaughlin and Clark, 2004).

The SAF itself has an estimated strike-slip offset of 128–144 km along the San Francisco peninsula within the past 13 Ma, with the most offset having occurred on the Pilarcitos fault—a strike-slip fault now abandoned on the Pacific plate (McLaughlin and Clark, 2004; Fig. 1). The San Gregorio fault has an estimated strike-slip offset of 115–170 km within the past 12 Ma (McLaughlin and Clark, 2004). The Zayante fault had an estimated 13 km of dip slip (southwest side up) during the period 90–61 Ma and another 4–5 km of dip slip in the Oligocene followed by a few kilometers of local dip slip (continued southwest side up) into the Pliocene (Clark, 1981; Bürgmann *et al.*, 1994; McLaughlin and Clark, 2004).

The epicenter of the 1989 $M_{\rm w}$ 6.9 Loma Prieta earthquake was about 6 km southwest of the mapped SAF zone and located on the Pacific plate. This location led to speculation on the identity of the active structure responsible for the earthquake (e.g., Dietz and Ellsworth, 1990, 1997; Eberhart-Phillips and Michael, 1998, 2004) and to the subject of the present study, with the question: Was the 1989 rupture on the main transform plate boundary fault, namely the SAF, or was it on a secondary fault?

3D VELOCITY MODEL

Lin and Thurber (2012) used 3D ray tracing and waveform cross-correlation techniques to generate a 3D velocity model and relocate aftershocks of the Loma Prieta earthquake. Their 3D velocity model relies on the use of composite events (Fig. 2a), obtained from closely spaced events that have highly correlated residuals in which random picking error dominates. The composite event location is the centroid of all similar events within a given radius. In this method, the earthquakes within a predefined distance are used to generate source-specific station terms (SSSTs), which are the averages of arrival-time residuals of all the events in the group recorded by each station (Richards-Dinger and Shearer, 2000; Lin and Shearer, 2005; Lin, Shearer, and Hauksson, 2007). Composite picks are obtained from adding the SSSTs to theoretical travel times calculated from a 1D velocity model. Lin and Thurber (2012) used 485 composite events (Fig. 2a) with an average of 22 contributing picks (P and S picks) per event. They estimated that random picking errors were reduced by 79% using this method. The advantage of this method compared to traditional master event methods is that it can result in a more uniform event distribution, greater number of picks per event, especially S picks, and reduced random picking errors (Lin et al., 2007). The relative location accuracies of the aftershocks were further improved using differential times from waveform cross correlation. To constrain the shallow crustal structure and absolute event locations, they assembled P-wave arrival times from active-source data cited by Brocher et al. (1992) and Eberhart-Phillips (1991). Resulting epicenters are shown near Loma Prieta in Figure 2b.

2D VELOCITY MODEL

The active sources referenced earlier were recorded in 1991 on a relatively dense seismic profile that extended approximately 25 km across the epicentral area of the Loma Prieta earthquake, from Aptos, California, northeastward to Calero Reservoir (Figs. 1, 2a,b; Catchings et al., 2004). Four inline shots were spaced approximately 5 km apart, and 161 receivers were deployed along the profile. The average receiver spacing was approximately 160 m. The arrival times were inverted in this study using the method of Hole (1992) to obtain a seismic velocity model (Fig. 3a). This model is characterized by (a) relatively low near-surface velocities southwest of the SAF that persist to a depth of about 3 km, (b) relatively high near-surface velocities at the SAF that persist to a depth of about 4 km, and (c) moderately low near-surface velocities between the SAF and Berrocal fault that persist to a depth of about 4 km. The major features of this model agree well with those of the model derived from these same arrivals by Catchings et al. (2004).

COMPARISON OF 2D AND 3D VELOCITY MODELS

A cross section through the 3D seismic velocity model of Lin and Thurber (2012) is shown in Figure 3b. This model is

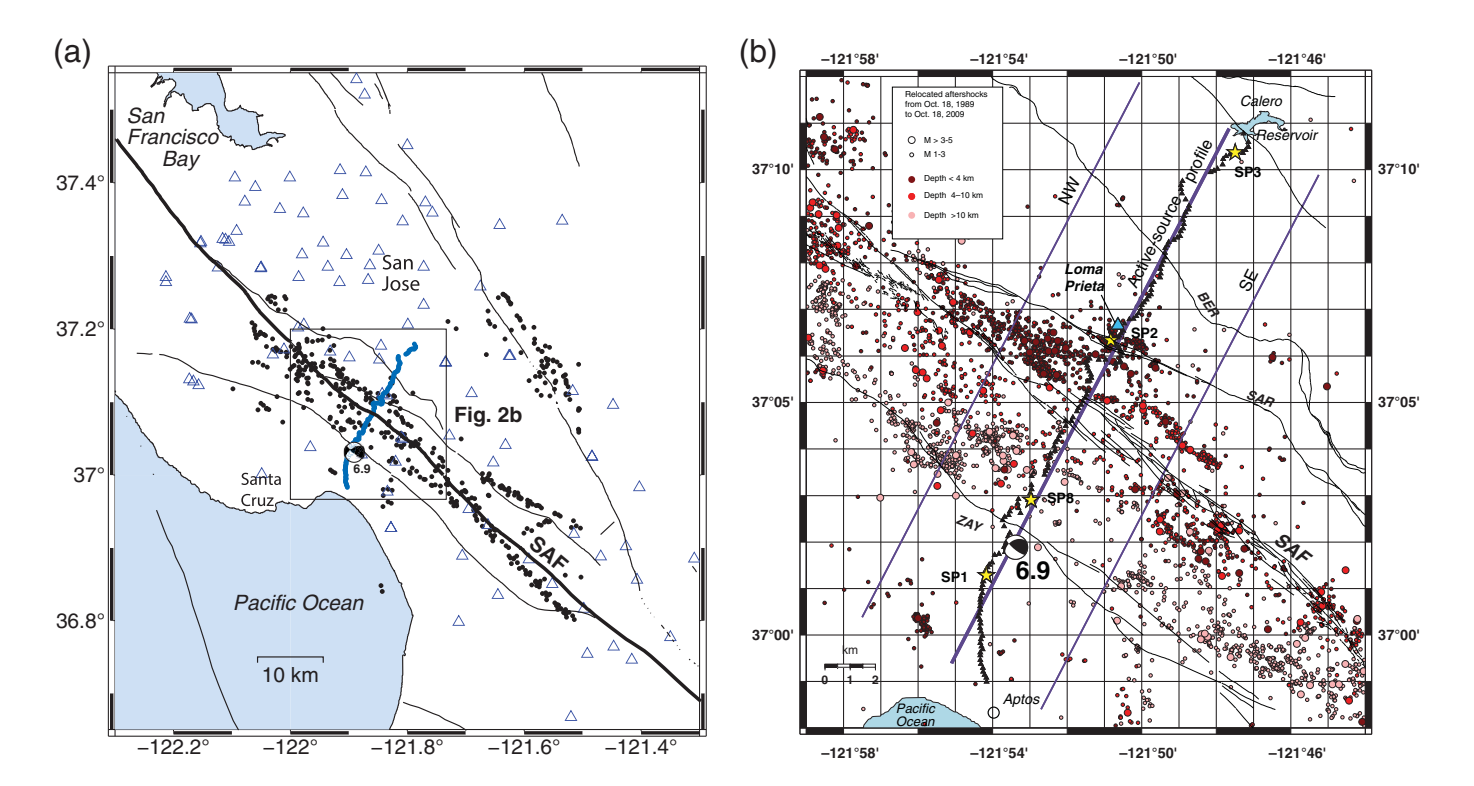


Figure 2. Map of Loma Prieta area showing permanent and portable seismic stations and "composite events" for Loma Prieta aftershocks. (a) Black dots, composite events from Lin and Thurber (2012), see 3D Velocity Model section; focal mechanism plot, NCSN focal mechanism of mainshock plotted at 3D relocation; blue open triangles, NCSN seismic stations used in Lin and Thurber (2012); smaller blue filled circles, portable seismic stations of active-source seismic profile of Catchings *et al.* (2004); black lines, faults; SAF, San Andreas fault. (b) Relocated aftershocks of 1989 $M_{\rm w}$ 6.9 Loma Prieta earthquake from Lin and Thurber (2012) and active-source seismic profile of Catchings *et al.* (2004). Filled circles, relocated

aftershocks from 20 yr period, 18 October 1989 to 18 October 2009; circle size, magnitude (see explanation); circle color, depth (see explanation); focal mechanism plot, NCSN mainshock focal mechanism plotted at 3D relocation; small filled black triangles, portable seismic stations of active-source seismic profile; yellow stars, shot points; heavy black line, least-squares fit to active-source profile; light black lines, profiles NW and SE of active-source profile for seismic cross sections (see Relocated Aftershocks section); blue triangle, Loma Prieta (peak), high point on profile; irregular black lines, faults from Jennings and Bryant (2010): BER, Berrocal fault; SAF, San Andreas fault; SAR, Sargent fault; and ZAY, Zayante fault.

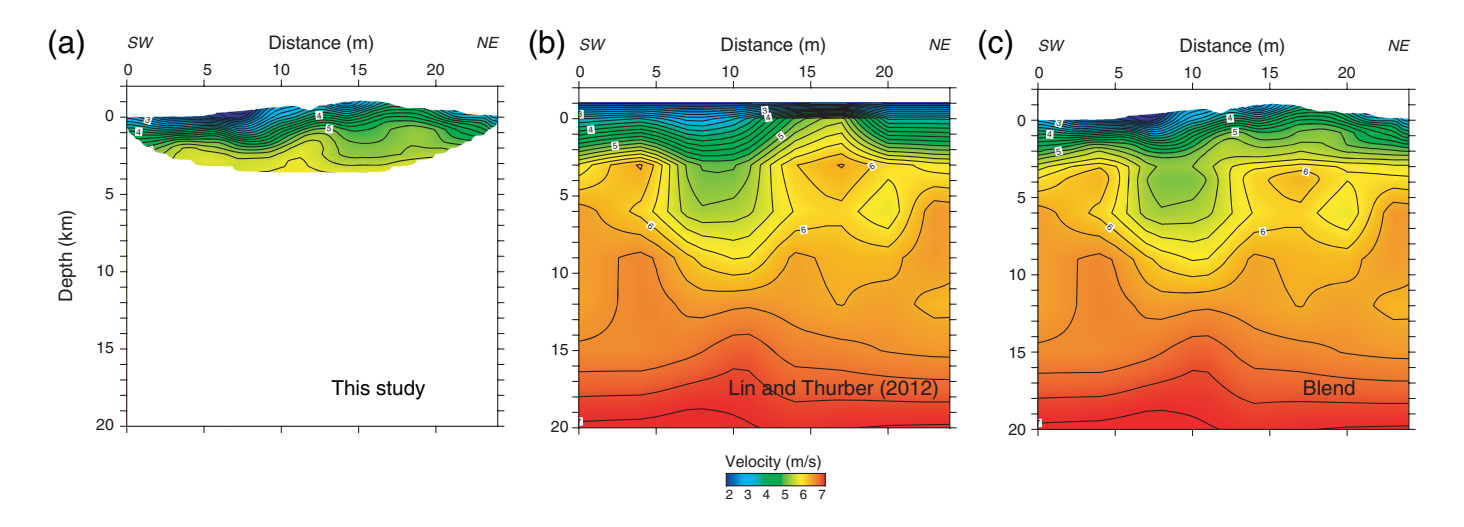


Figure 3. Velocity models from (a) this study, (b) Lin and Thurber (2012), and (c) a blend of (a) and (b) (see Comparison of 2D and 3D Velocity Models

section). Velocity contours labeled every 1 km/s.

characterized by (a) relatively high velocities from the southwest edge of the model to the Zayante fault below about 3 km depth, with a northeast boundary that appears to dip to the southwest, (b) relatively low near-surface velocities between the Zayante fault and SAF zone (which includes the Sargent fault) that persist to 10–12 km depth (La Honda block), and (c) moderately high near-surface velocities between the SAF zone and Berrocal fault that persist to 10–12 km depth.

There are some contrasts in the upper crust between the 2D and 3D models. To both migrate reflections detected on the active-source seismic line (see subsequently), where we need a velocity model extending to more than 10 km depth, as provided by the 3D model, and to improve accuracy of near-surface velocities, which are better constrained in the 2D model, we "blended" the two models. The 2D model was weighted 1 from the surface to 2 km depth, and the weight was tapered downward to zero between 2 and 5 km depth. The 3D model was weighted 0 from the surface to 2 km depth, the weight was tapered upward from 0 to 1 between 2 and 5 km depth, and the weight was 1 below 5 km depth. The resultant model is shown in Figure 3c.

RELOCATED AFTERSHOCKS

Aftershocks before and after high-precision relocation by Lin and Thurber (2012) are compared in Figure 4. Hypocenters from the catalog of the Northern California Seismic Network (NCSN, Fig. 4a) that plot within ±2 km of the active-source seismic line (see Fig. 2b) were located using two (similar) 1D velocity models: one model for the North American plate and one model for the Pacific plate (Oppenheimer et al., 1993). Hypocenters located with the 3D velocity model and waveform cross correlation by Lin and Thurber (2012) within the same ±2 km strip are shown for comparison in Figure 4b. The latter hypocenters locate shallower in depth and farther southwest than the NCSN hypocenters owing to lower velocities in the 3D model for the region of the La Honda block compared to velocities in the 1D model for the Pacific plate. (The 1D model, of course, does not contain the La Honda block and has higher velocities at most depths.) Importantly, the hypocenters of Lin and Thurber (2012) form three relatively well focused clusters, including steeply dipping curvilinear clusters below (but slightly northeast of) both the SAF (2-6 km depth) and Sargent fault (2-4 km depth) and a more diffuse group along the southwest-dipping presumed main rupture (10-16 km depth; compare with Dietz and Ellsworth, 1990, 1997). Similar but more poorly focused features are seen in prior 3D velocity models and aftershock relocations by Foxall et al. (1993), Eberhart-Phillips and Michael (1998, 2004), and Thurber et al. (2007).

Tracing features of the 3D velocity model and aftershocks in cross sections northwest and southeast of the active-source seismic line (Fig. 5a,b, respectively) indicates similarities and

differences. In both the cases, velocity boundaries persist below about 3 km depth beneath the Zayante fault, SAF and Sargent fault, and Berrocal fault, but the depth of the low-velocity region between the Zayante fault and SAF and Sargent fault (the La Honda block) is diminished southeast of the active-source line by about 2 km (Fig. 5b). Northwest of the active-source line, aftershocks above 5 km depth do not define separate curvilinear features beneath the SAF and Sargent fault but cluster more diffusely between those two faults (Fig. 5a). Below 9 km depth, however, the aftershocks form a well-focused dipping feature (9-16 km depth) along the presumed main rupture (Dietz and Ellsworth, 1990, 1997). Southeast of the active-source line, aftershocks form less well-focused features, with a diffuse cluster centered at 4 km depth southwest of the SAF, a diffuse southwest-dipping cluster at 9-15 km depth, and an enigmatic sharp, steeply northeast-dipping cluster at 7-9 km depth below the SAF (Fig. 5b). In the cross sections along the active-source seismic line (Fig. 4b) and the one to the northwest (Fig. 5a), aftershocks appear associated with the steep northeast boundary of the region of low velocities between the Zayante fault and the SAF and Sargent fault (the La Honda block). In the southeast cross section (Fig. 5b), association of aftershocks with the steep northeast velocity boundary is less clear.

In regions farther southeast than the southeast line, aftershocks and modeling of aeromagnetic data suggest that the SAF tends to become more planar and has a southwest dip (Jachens and Griscom, 2004, their figs. 4, 15; Lin and Thurber, 2012, their fig. 6H–J). In regions farther northwest than the northwest line, aftershocks indicate a continued complex shape similar to that along the active-source line (Lin and Thurber, 2012, their fig. 6A–C).

V_P/V_S

 V_P/V_S values calculated by Lin and Thurber (2012) are reproduced along the active-source line in Figure 6. Values less than 1.70 form a very noticeable region that coincides with the region of low velocities between the Zayante fault and the SAF and Sargent fault (La Honda block). Higher values of V_P/V_S are seen both southwest and northeast of this low-velocity region. V_P/V_S values to the northeast reach over 1.80. V_P/V_S values are valuable in interpreting rock type (see subsequently).

POTENTIAL FIELD DATA

Potential field data collected in the Loma Prieta region by the U.S. Geological Survey (USGS) following the Loma Prieta earthquake (Abrams *et al.*, 1991) were modeled by Jachens and Griscom (2004) along an aeromagnetic profile parallel to but 5 km southeast of our active-source seismic line (Fig. 7; near the southeast line of Figs. 1, 2b). Between the SAF and Berrocal fault, they modeled two bodies of

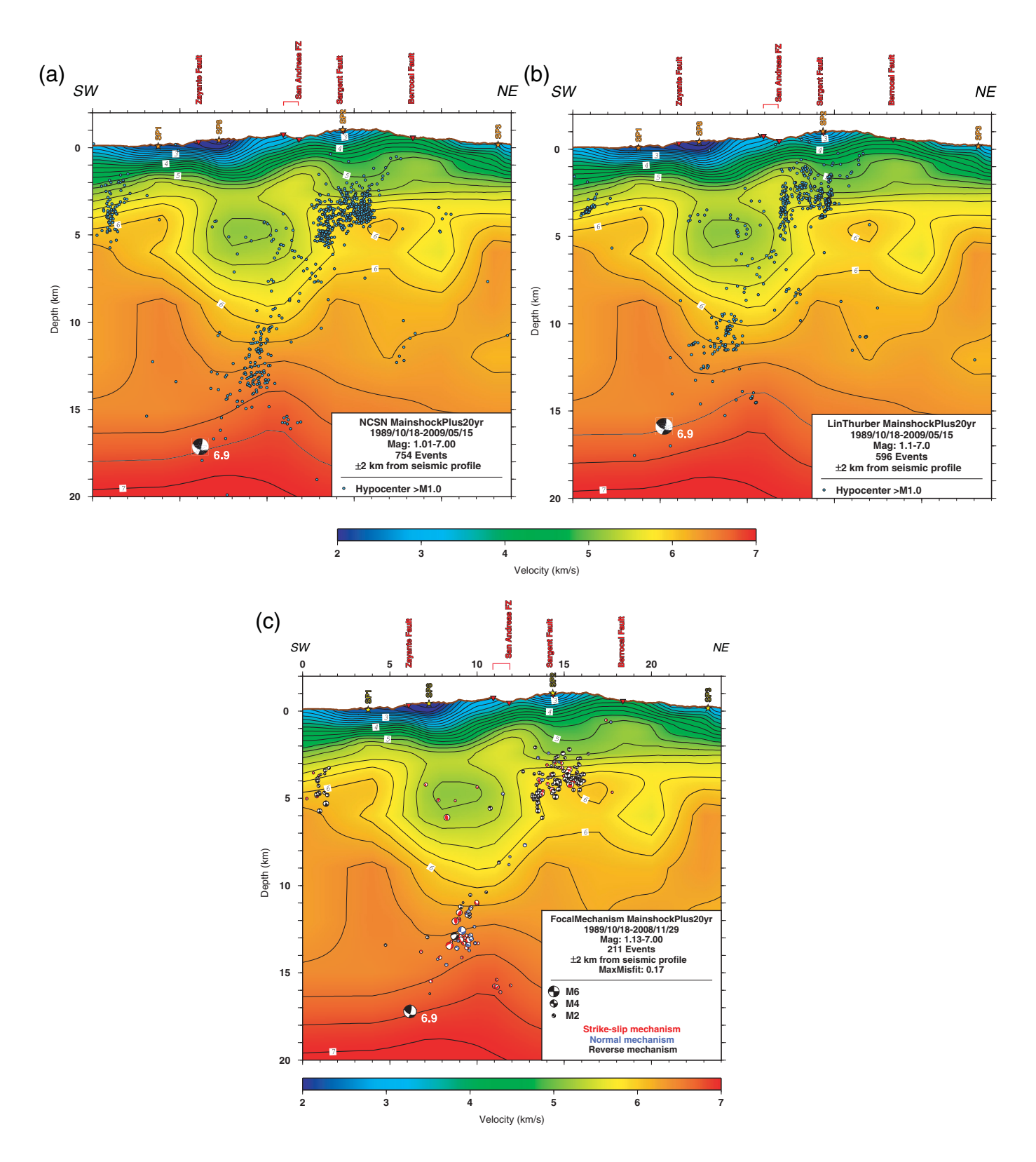
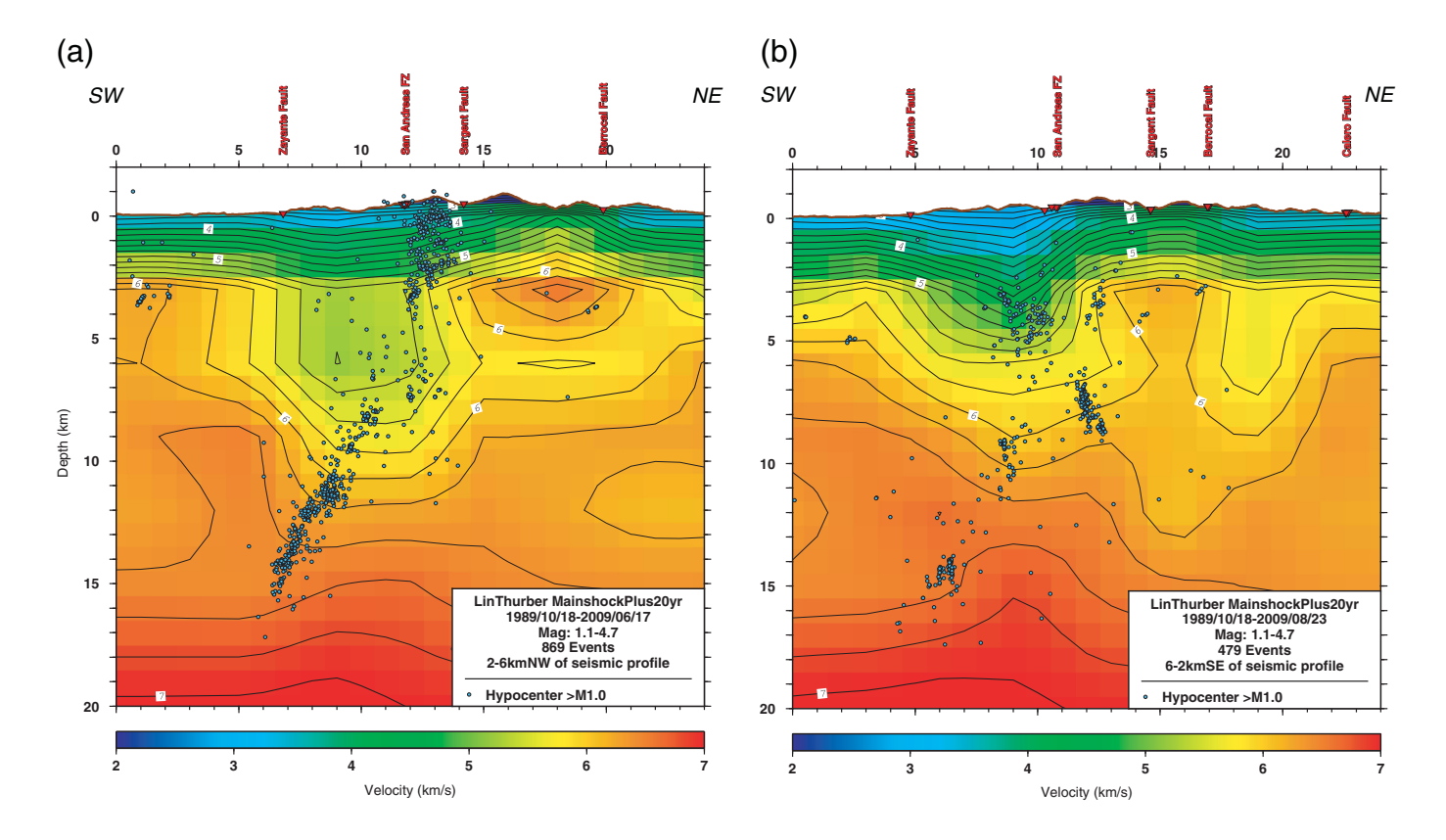


Figure 4. (a) Original hypocenters (filled blue circles) within ± 2 km of least-squares fit to active-source line (see Fig. 2b) from catalog of NCSN. (b) Relocated hypocenters (filled blue circles) within same region from Lin and Thurber (2012). (c) Focal mechanisms from NCSN within the same region plotted at NCSN hypocenters. Focal mechanisms include the best three-fourth of mechanisms with focal-plane fit value of <0.17 (see Reasonberg and Oppenheimer, 1985). Note that SAF zone indicated above

each figure spans nearly a 1 km interval (see Fig. 2b), with much of it covered near our active-source profile by landslide material (see Fig. 8b, cross section). Principal trace is on right (below words San Andreas fault zone). In this figure, hypocenters are plotted on blended velocity model of this study (Fig. 3c), rather than on original velocity models with which they were located (see Relocated Aftershocks section for explanation of those models), to provide same model reference features and enable comparison.



interpreted Jurassic ophiolitic rocks with a magnetization of 0.00040 (in electromagnetic units per cubic centimeter) that dip southwestward (see Fig. 7, geologic unit Jou). The largest body was interpreted to bottom at an interpreted southwestdipping Berrocal fault. Between the Zayante fault and SAF, in the La Honda block, they modeled a couple of small, nearsurface bodies of Pliocene Purisima Formation (sandstone), which is magnetic. Importantly, a small body of Purisima Formation adjacent to the SAF (seen in outcrop immediately southeast of our active-source seismic line in Fig. 1) led them to model an initial northeast dip for the SAF. In their modeling, the fault dip changed with depth in the upper few kilometers to a steep dip and then joined the presumed southwest-dipping rupture for the Loma Prieta earthquake at about 10 km depth. See also the Near-surface northeast dip of **SAF** section.

We projected the magnetic bodies of Jachens and Griscom (2004; Fig. 7) northwestward to our seismic line, and then adjusted shapes and magnetizations to fit aeromagnetic data along our profile (Fig. 8a). The data along our seismic profile resemble in many ways the data modeled by Jachens and Griscom (2004) with respect to the location of peaks and troughs, although amplitudes differ (compare Figs. 7, 8a, data panels).

When we modeled gravity along our seismic profile, we referred to gravity models of Jachens and Griscom (2004; their figs. 1, 3, 5, 9, 16) across the La Honda block, which consists of a deep basin of Cenozoic sedimentary rocks. In their study, vertical density structure for the sedimentary

Figure 5. Relocated hypocenters (filled blue circles; Lin and Thurber, 2012) within ± 2 km of lines located (a) 4 km NW of and (b) 4 km SE of active-source line (see Fig. 2b). These models show original 1 km \times 1 km inversion gridding.

rocks was determined using the relationship of Gardner et al. (1974) and the velocity model of Foxall et al. (1993). The density values were adjusted somewhat using the densities of samples collected from surface outcrops and from cores extracted from a deep drill hole in the La Honda block. The gravity models of Jachens and Griscom (2004) contained flat layers with density increasing with depth for the region of the La Honda block. For our initial gravity model, this distribution of density produced a gravity minimum approximately 2 km northeast of the observed minimum (see Fig. 8a, data panels; see also supplemental material). Warping these flat layers in accordance with a geologic cross section drawn near our active-source seismic line by McLaughlin et al. (2004; see Figs. 1, 8b), in which a syncline depresses younger (and lower-velocity and lower-density) sedimentary rocks in the southwest half of the La Honda block, and anticlines and faulting uplift older sedimentary rocks in the northeast half, permitted a closer match to the observed gravity minimum (Fig. 8a, data panels).

Comparing the geologic cross section with the aeromagnetic model (Fig. 8b) in the region northeast of the SAF reveals only a general correlation whereby bodies with relatively high-magnetic susceptibility (S = 0.00251-0.01508, in

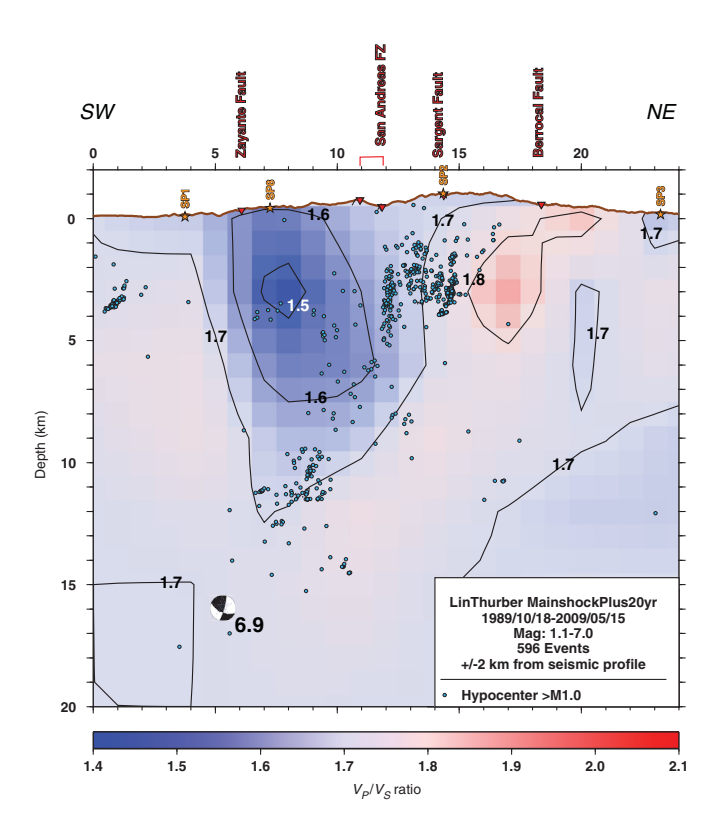


Figure 6. V_P/V_S (see color bar) and hypocenters (filled blue circles; Lin and Thurber, 2012) within ± 2 km of active-source line. Mainshock focal mechanism from NCSN plotted at 3D relocation. This model shows original 1 km \times 1 km inversion gridding.

dimensionless SI units) approach the surface at Loma Prieta peak, which is underlain by ophiolitic rocks, including mafic to intermediate flows and intrusions (geologic units Jom, Fig. 1; Jov, Fig. 8b) and cumulate ultramafic to gabbroic rocks (geologic unit Jou, Figs. 1, 8b). As in the aeromagnetic model of Jachens and Griscom (2004; fig. 7), a body of buried magnetic Purisima Formation requires a steep northeast dip of the SAF near the surface (see Fig. 8a,b; geologic unit Tp; S = 0.00151).

Modeling of potential field data is discussed further in the supplemental material.

REFLECTIONS

Active-source seismic data acquired after the Loma Prieta earthquake by Catchings *et al.* (2004; fig. 2a,b) have been investigated for upper crustal velocity structure, as described earlier and also for low-fold reflections, although the acquisition geometry was not ideal for reflection detection. As described previously, we blended the 2D and 3D velocity models to generate a model needed to migrate detected reflections (see Fig. 3c).

The dominant recorded seismic frequencies from the explosions are 10–20 Hz (Fig. 9), and dominant velocities in the uppermost 5 km are 4–5 km/s (Fig. 3a,c). The optimum

receiver spacing should average ~80 m to sample four data points per wavelength, but given an average receiver spacing of ~160 m along the Loma Prieta profile, the geometry of this profile is not ideal for imaging reflectors without care to avoid aliased phase correlations. One can calculate the maximum seismic frequency $(f_{\rm max})$ above which aliasing in phase correlations is likely from the equation:

$$f_{\text{max}} = v/(4 \times 0.16 \text{ km} \times 0.5) \sim 13-16 \text{ Hz},$$
 (1)

in which ν is the average seismic velocity (km/s) along ray paths, and 0.16 km is the average station spacing (e.g., Yilmaz, 1987). We make use of $f_{\rm max}$ in choosing a band-pass filter for our seismic data, namely 2–16 Hz. Zhang *et al.* (2018) used a band-pass filter of 10–20 Hz, incorporating reflections with slightly higher frequencies than those used in this study.

Preprocessing steps for our seismic data included dead trace removal, non-zero mean of amplitudes in a seismic trace (DC) removal, top mute, automatic gain control (2 s operator length), spectral whitening, band-pass filtering (2-16 Hz), and deconvolution (80 ms operator length). The processing method of Bauer et al. (2013) was then applied to detect possible reflections in the time domain (record sections; Fig. 10a). It uses slant-stack processing, draws lines at the detected phases (Fig. 10b), and migrates the lines in the depth domain (Fig. 10d). Detection includes coherence and amplitude analyses, with required thresholds of 0.5 and 0.1 (absolute value of normalized amplitude), respectively. Coherences (Fig. 10c) are multiplied by amplitudes to obtain quality (or reliability) factors called amplitude-weighted coherences that are represented simply by line length (see explanation in the depth panel, Fig. 10d). The method detects and migrates both subhorizontal reflections (ones with normal moveout) and also steep reflections (ones with reverse moveout). Slowness filters are used for both types of reflections (absolute value of slowness <0.11 s/km for the former and slowness × offset <0 for the latter) to eliminate unwanted phases, including refracted P and S waves, surface waves, and multiples. See Bauer et al. (2013; their fig. 6 for a demonstration of filtering), and see Appendix for a description of detection and migration.

Reflections from SP3 are shown in both the time and depth domains in Figure 10. Reflections of interest are labeled A and B. Reflections A, strong wide-angle reflections, are easily detected by the method described earlier, and these are really the only significant, interpretable reflections detected. These migrate to subhorizontal reflections at around 10 km depth in the region between the SAF and Zayante fault (Fig. 10d). Reflections B have reverse moveout, are relatively weak, and are examples of steep reflections (Fig. 10b). These B reflections migrate to the upper crust in the vicinity of the SAF (Fig. 10d) but are not distinctive

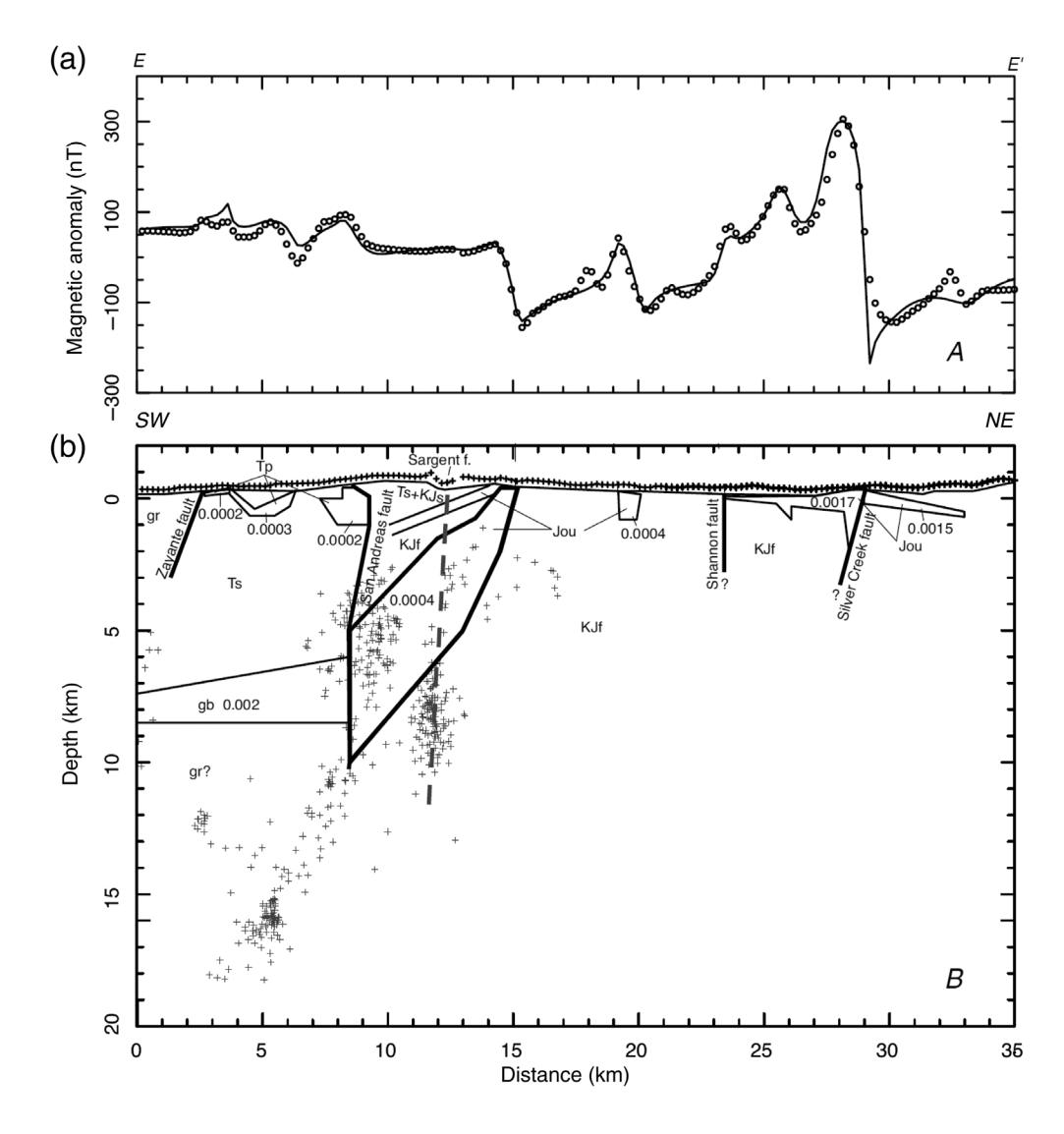


Figure 7. Figure 13 of Jachens and Griscom (2004; public domain) showing magnetic modeling along a profile approximately 5 km southeast of our main seismic line (their profile E–E′). (a) A: small circles, gridded observations; solid line, calculated magnetic anomaly. (b) B: modeled magnetic bodies. Numbers on magnetic bodies are magnetizations in electromagnetic units per cubic centimeter. Pluses, aftershocks, from 18 October 1989 to 1991 (within 2.5 km of profile), from NCSN. gb, gabbro; gr?, granitic rocks?; Jou, Jurassic ophiolitic rocks undivided; KJf, Cretaceous and Jurassic Franciscan Complex; Tp, Tertiary (Pliocene) sedimentary rocks; and Ts, Tertiary sedimentary rocks.

among other weak, steep reflections, such as ones seen farther southwest in the La Honda block. However, reflections from other shot points, as seen in Figure 11, are seen in the same vicinity, both above and below B.

INTERPRETATION AND DISCUSSION

Combining all the aforementioned data permits the interpretation shown in Figure 12.

Rock composition

Rock composition can be interpreted from multiple data sets, including geologic data from outcrops and oil wells (Figs. 1, 8b),

seismic velocities (Fig. 3), and potential field data analyses (Fig. 8a,b).

From the Zayante fault to the southwest, Salinian granitic and metamorphic rocks of the Ben Lomond block (e.g., Ross, 1970, 1978) are identified from outcrops and well data below a thin (<3 km) cover of Cenozoic sedimentary rocks. Seismic velocities below ~3 km depth (>5.8 km/s; Fig. 3c) are consistent with granitic and pelitic metamorphic rocks (e.g., Clark, 1966; Mavko *et al.*, 1998).

Between the Zayante fault and the SAF, within the La Honda block, Cenozoic clastic sedimentary and volcanic rocks are identified from outcrop and well data (Figs. 1, 8b). Relatively low velocities (<5.8 km/s; Fig. 3c) are generally consistent with clastic sedimentary and volcanic rocks (e.g., Clark, 1966; Mavko et al., 1998). Relatively low V_P/V_S ratios (<1.7; Fig. 6) are also generally consistent with quartz-rich sedimentary rocks (Mavko et al., 1998). For example, relatively clean sandstone (water saturated) has a V_P/V_S ratio averaging as low as 1.50 and as high 1.68. As clay content increases, the V_P/V_S ratio averages increase to as much 1.74. Relatively densities $(2400-2600 \text{ kg/m}^3)$;

Fig. 8b) are consistent with clastic sedimentary and volcanic rocks (e.g., Clark, 1966; Gardner et al., 1974; Mavko et al., 1998). We found it best to model these rocks with the synclinal and anticlinal geometry shown in an oil-well-controlled geological cross section across the La Honda block by McLaughlin et al. (2004), whereby younger, lower-density sedimentary rocks are depressed in the southwest part of the La Honda block, and older, higher-density sedimentary rocks are uplifted in the northeast part of the La Honda block (Fig. 8b). We modeled the increase in seismic velocity and density at ~10–12 km depth (from 6.0 to 6.4 km/s [Fig. 3] and 2670–2870 kg/m³ [Fig. 8a]), the increase in magnetic

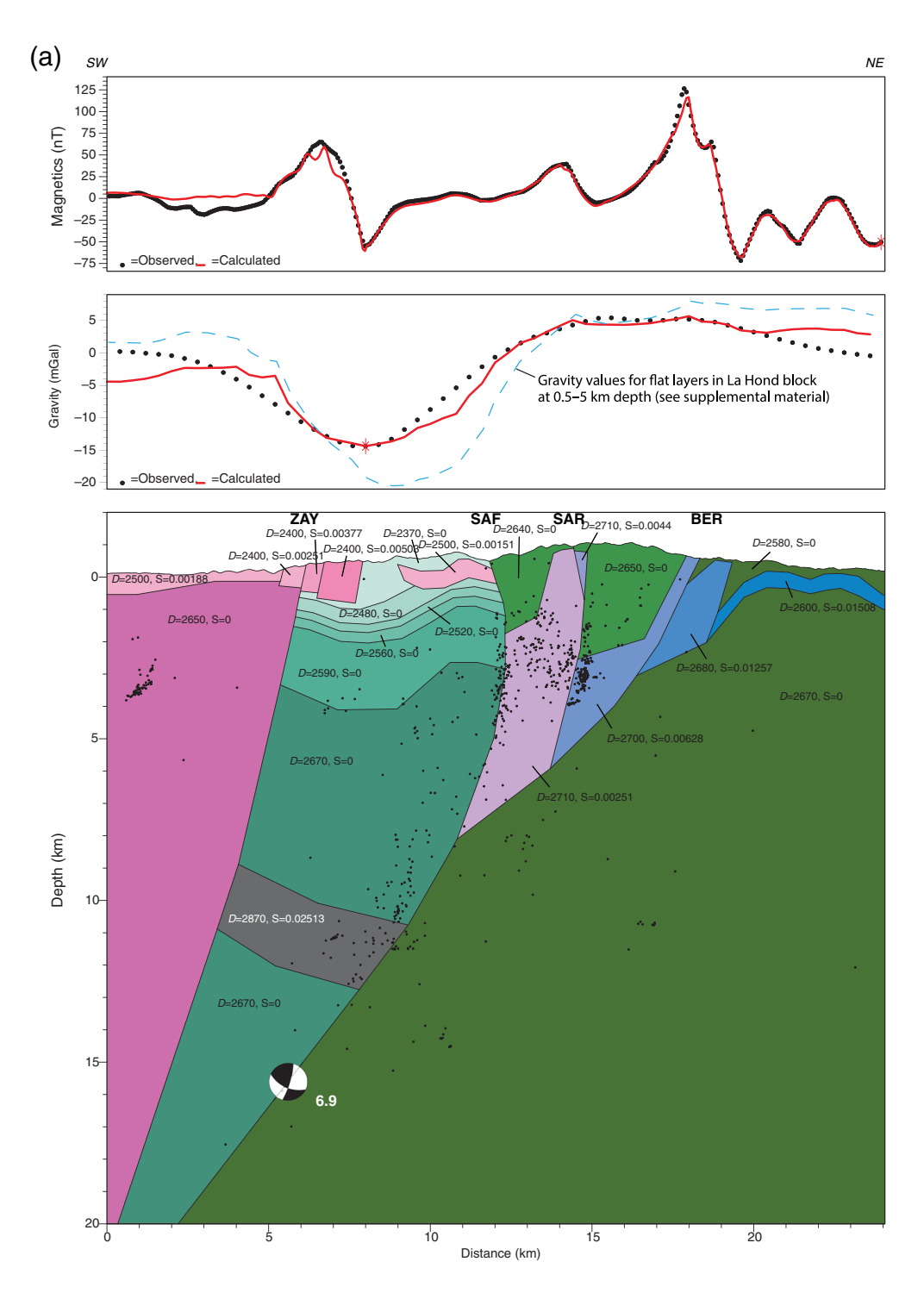


Figure 8. (a) Model of aeromagnetic and ground-based gravity data along active-source profile. Black dots represent seismicity (Lin and Thurber, 2012) within ± 2 km of profile. Mainshock focal mechanism from NCSN plotted at 3D relocation. D, density (kg/m³); S, magnetic susceptibility (SI units [dimensionless]). Bodies are colored arbitrarily to distinguish ones with different density and susceptibility values. (b) Comparison of potential field model of panel (a) with geologic cross section S6 of McLaughlin *et al.* (2004). See Figure 1 for location of cross section. From cross section, geologic contacts (black) and rock bodies likely to be magnetic (Jov, Jou, Jos—purple) are superposed on potential field model for direct comparison. In addition to rocks shown as likely to be magnetic, rocks within Franciscan Complex may also be magnetic, including basalt and serpentine, but their positions are unknown. Heavy white lines, faults interpreted from aftershocks (black dots), and magnetic contrasts include Zayante f., SAF, Sargent f., and Berrocal f. See also Figure 12. (*Continued*)

susceptibility (from 0 to S = 0.02513 in dimensionless SI units; Fig. 8a), and the presence of a strong reflective horizon (Fig. 10d, Figs. 11, 12, reflectors A) with a body interpreted as the Logan gabbro, although common velocities and densities expected for gabbro are typically a bit higher (\sim 6.5-6.8 km/s and $2900-3000 \text{ kg/m}^3$, respectively). Jachens and Griscom (2004) modeled this body with a generic wedge shape (Fig. 7), and, indeed, the shape of this body is poorly constrained (see supplemental material). The Logan gabbro has a Jurassic age (161-165 Ma; James et al., 1994) and may or may not represent an ophiolitic body at the base of the Cenozoic La Honda sedimentary basin.

It is interesting that a potential field model of the Eagle Rest Peak gabbro, in the San Emigdio Mountains at the south end of the San Joaquin Valley, possibly correlated to the magnetic body at the bottom of the La Honda block in our model, has somewhat similar potential field properties, $D = 2850 \text{ kg/m}^3$ and S = 0.01000 SI units, with basement rocks ($D \sim 2670 \text{ kg/m}^3$; granitic and metamorphic rocks[?]) beneath it and sedimentary rocks above it (Fuis et al., 2012, their appendix A).

Faulted Mesozoic accretionary rocks, Mesozoic sedimentary rocks of the California Great Valley Sequence, and Tertiary sedimentary rocks extend from the SAF to the northeast, as summarized in McLaughlin and Clark (2004) and McLaughlin et al. (2004). The Mesozoic accretionary rocks include the Franciscan

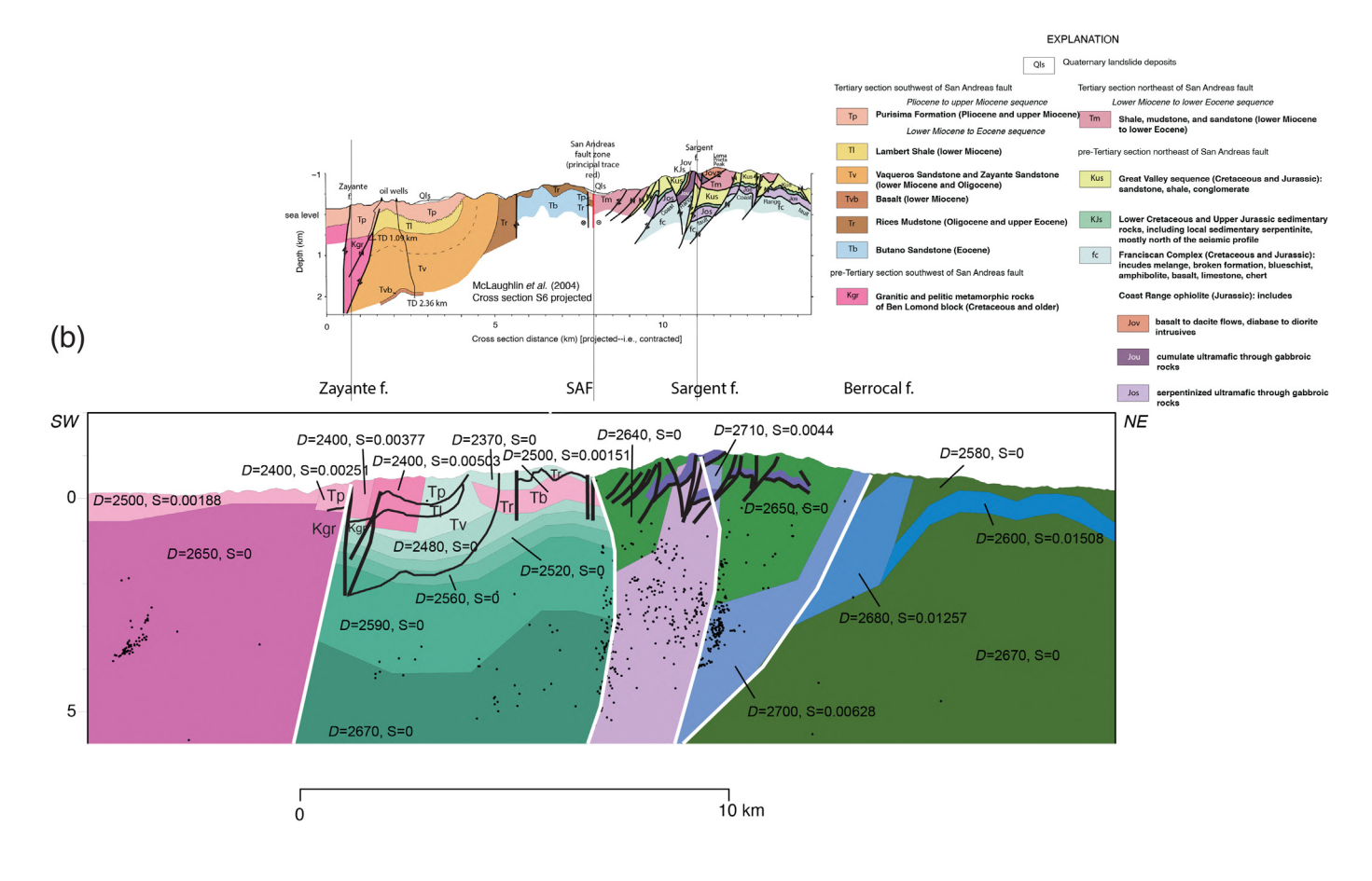


Figure 8. Continued

Complex (basalt, chert, greenstone, high-pressure metamorphic rocks, and shale, disposed in blocks and mélange) and ophiolitic rocks (mafic to intermediate extrusives and intrusives, cumulate ultramafic to gabbroic rocks, and serpentinized ultramafic rocks). Faults include both compressional and extensional faults; the Coast Range fault is a prominent extensional fault. These rocks are mostly older and more mafic than the Cenozoic sedimentary rocks of the La Honda block, and hence are higher in velocity (up to 6.0 km/s; Fig. 3c) and density (2640-2710 kg/m³; Fig. 8a,b). The presence of mafic and serpentinized rocks produces higher modeled magnetic susceptibility (S = 0.00251-0.01508 SI units). Given the structural complexity of these rocks, we are able to model only general properties, such as a velocity and density high northeast of the SAF (Fig. 8a), and a magnetic susceptibility high at Loma Prieta peak, where ophiolitic rocks outcrop (Fig. 8b). Higher magnetic susceptibility is also modeled from 2 to 8 km depth along the northeast side of the interpreted SAF and from the surface to 7 km depth above the interpreted Berrocal fault, similar to the geometry inferred by Jachens and Griscom (2004; Fig. 7).

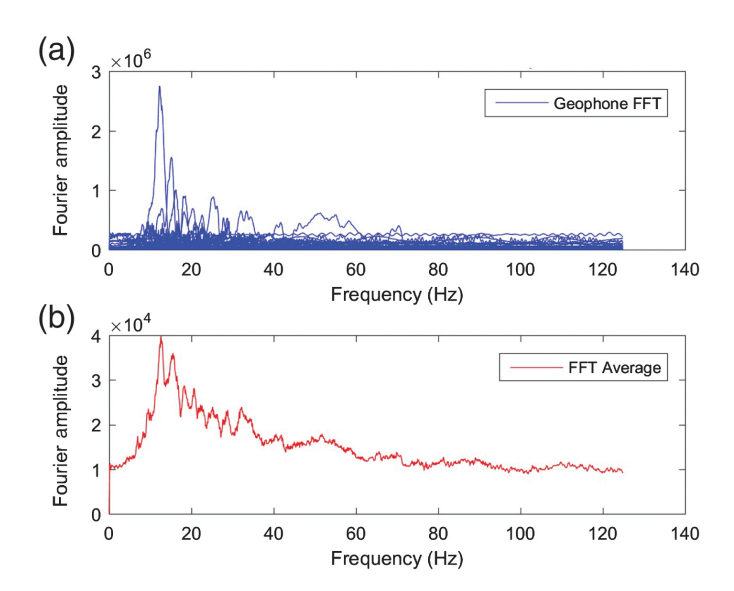


Figure 9. Fast Fourier transforms (FFTs) of raw data for (a) each individual trace in active-source seismic profile and (b) average of all traces. Dominant frequencies of our explosions are 10–20 Hz. Frequencies above 16 Hz are not used to avoid possible aliasing (see equation 1).

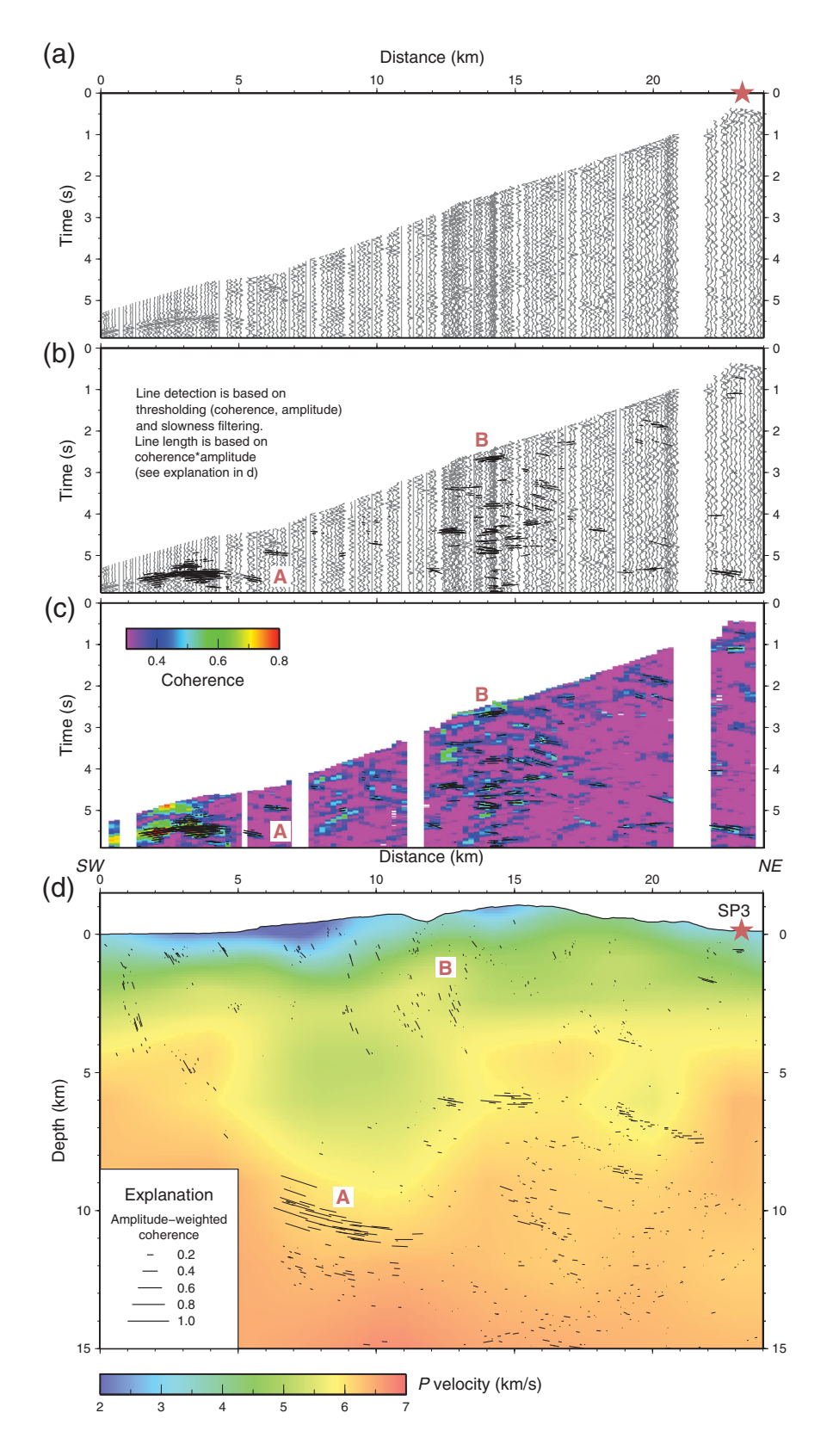


Figure 10. (a) Time section of seismic traces from SP3 (see Fig. 2b for location). Preprocessing steps for seismic data included dead trace removal, non-zero mean of amplitudes in a seismic trace (DC) removal, top mute, automatic gain control (2 s operator length), spectral whitening, band-pass filtering (2–16 Hz), and deconvolution (80 ms operator length). (b) Reflections (black lines) were detected using (c) coherence, amplitude, and slowness analysis and (d) migrated using algorithm of Bauer *et al.* (2013) (see Reflections section and Appendix). Reflections labeled A, B are discussed in Reflections section. Quality (or reliability) factors for reflectors, called amplitude-weighted coherences, are represented simply by reflector line length, as shown in explanation for (d).

Structure

We have been able to map faults using relocated aftershocks for active faults (SAF, Sargent fault; Figs. 4b, 8a,b, 12), seismic velocity and density boundaries for both active and inactive faults (Zayante fault and SAF; Figs. 4b, 8b, 12), and magnetic susceptibility boundaries for selected faults (SAF, Sargent fault, Berrocal fault; Fig. 8b). We have been able to interpret broad folds in the La Honda basin using model density data (Fig. 8b).

The relocated aftershocks of Lin and Thurber (2012) provide perhaps the clearest indicators of the SAF and Sargent fault that have been generated since occurrence of the Loma Prieta earthquake in 1989, although prior relocations, such as those of Dietz and Ellsworth (1990, 1997), Eberhart-Phillips and Michael (1998, 2004), and Thurber et al. (2007), produce diffuse images of these faults. The steep, curvilinear earthquake alignments beneath the surface traces of the SAF and Sargent fault in Figures 4b, 8a, and 12 are persuasive. These alignments are shifted slightly to the northeast of both the surface traces, conwith aeromagnetic sistent modeling that are best modeled with these shifts (Fig. 8a). We have connected the upper crustal alignment of aftershocks along the interpreted SAF with the approximate base of the more diffuse aftershocks below 6 km depth, avoiding to the extent possible reflections A, belonging to the mafic rocks at the base of the La Honda basin, and connecting with the relocated mainshock at about 16 km depth. We have chosen to interpret the SAF

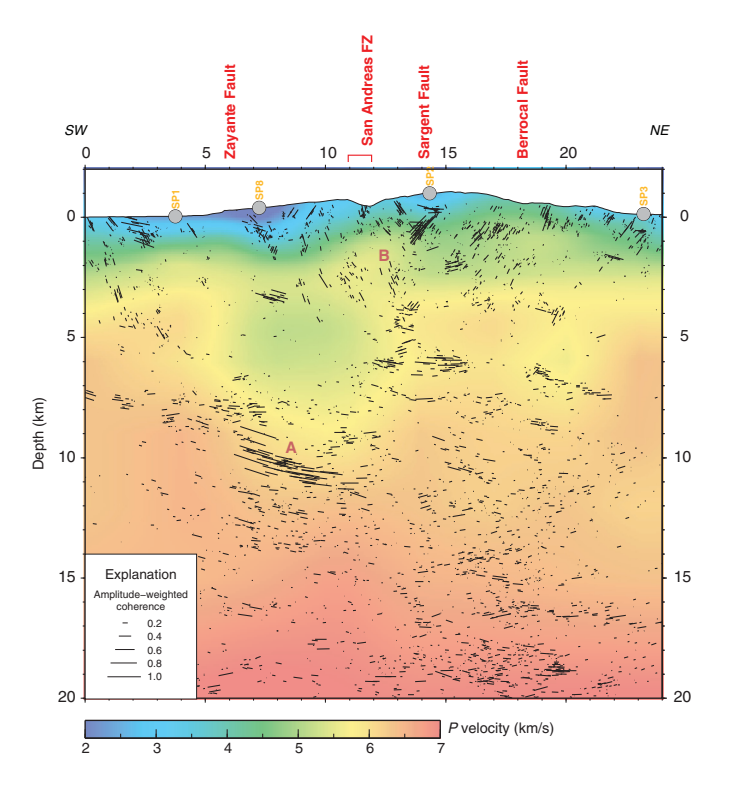


Figure 11. Reflections (black lines) from all four shot points. Reflections A, B are discussed in Reflections section. Note that SAF zone indicated at top spans nearly a 1 km interval (see Fig. 2b), with much of it covered near our active-source profile by landslide material (see Fig. 8b, cross section). Principal trace is on the right (below words San Andreas fault zone).

along the approximate base of the diffuse aftershocks between 6 and 16 km depth following the pattern of aftershocks elsewhere in California for reverse faults, where the aftershocks are interpreted to be located in the hanging walls of faults (e.g., Tsutsumi and Yeats, 1999, and Fuis *et al.*, 2003 for the 1971 M 6.7 San Fernando and 1994 Northridge earthquakes; Eaton, 1990 for the 1983 M 6.7 Coalinga earthquake). Our interpreted geometry for the SAF (Fig. 12) is similar to one of the interpretations of Dietz and Ellsworth (1990) whereby the fault bends sharply from a moderate dip below ~9 km depth to a vertical dip above that depth to connect with the surface trace of the SAF.

Reflections A. The gently northeast-dipping reflections at 9–12 km depth clearly represent layering with seismic discontinuities. These layers may represent igneous bodies within one or more ophiolites (see e.g., Spudich and Orcutt, 1980) or alternating deposits of sedimentary rocks, basalts, and submarine landslides. The presence of rocks with higher density, velocity, and magnetic susceptibility is required, as seen in our model (Figs. 8a, 12), and would most likely include mafic igneous rocks.

Steep reflections. Packages of short, steep reflections are modeled between the SAF and Sargent fault in the upper

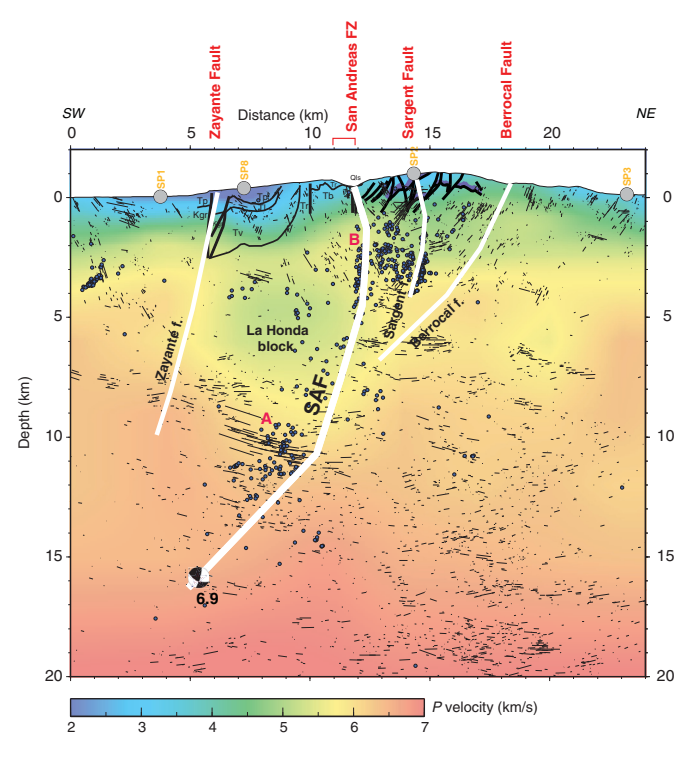
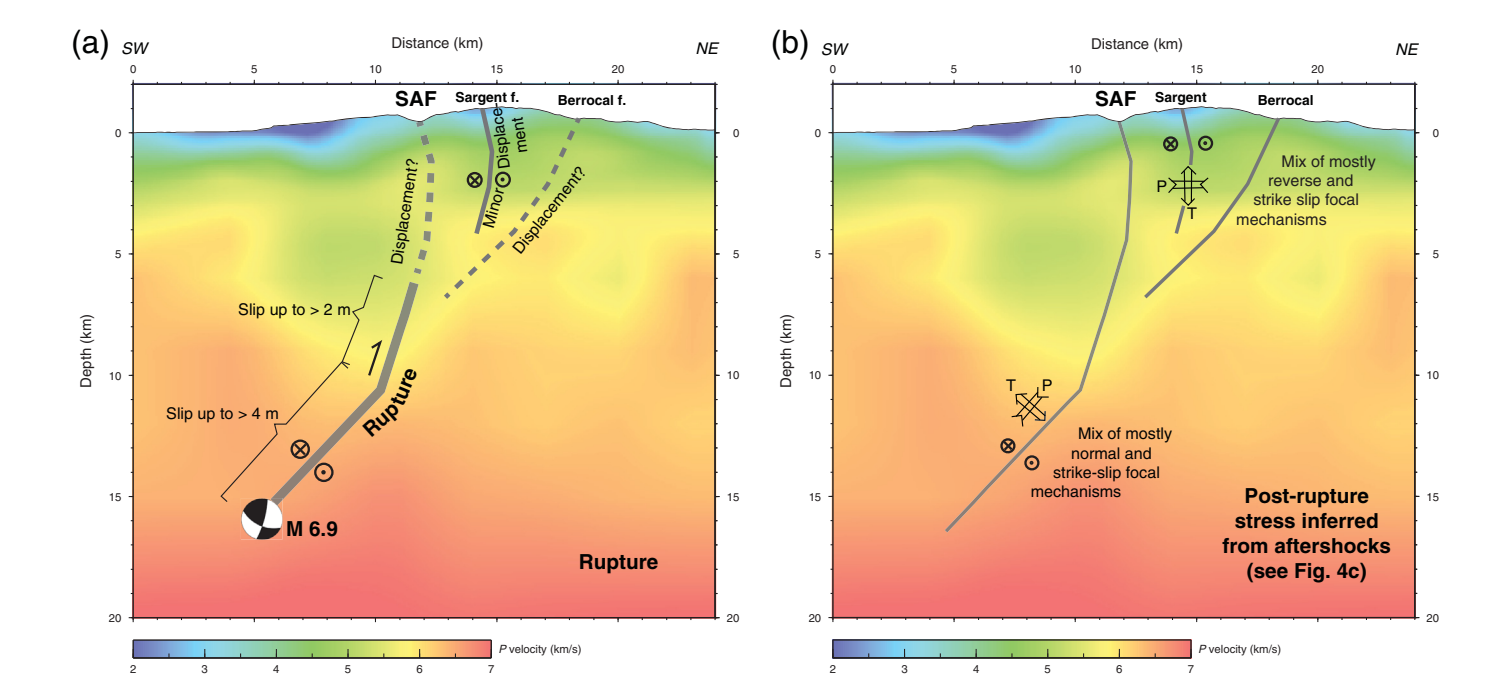


Figure 12. Interpretation of cross section along active-source profile from all data. From cross section of Figure 8b, geologic contacts and faults (black) and rock bodies likely to be magnetic (Jov, Jou, Jos—purple) are superposed on this velocity model for direct comparison. Black labels southwest of SAF, geologic unit abbreviations (see Fig. 8b); fine black lines, reflections from Figure 11; heavy white lines, faults interpreted from aftershocks (blue filled circles) and magnetic contrasts (see Fig. 8b): Zayante f., SAF, Sargent f., and Berrocal f. A, reflections from Figure 10 interpreted as possible ophiolitic(?) rocks at base of La Honda block; B, weak reflections at or near interpreted SAF. Mainshock focal mechanism from NCSN plotted at 3D relocation.

few kilometers or so of the crust, including reflections B (Fig. 11), and other examples can be seen to the northeast and southwest. These are puzzling but may represent (a) diffractions from steeply oriented velocity discontinuities or faults, (b) fluid-filled fractures including those generated by shaking and possible tectonic deformation that occurred during the Loma Prieta earthquake, or, in some cases, (c) possibly noise. For the first possibility, mapped faults in this area, interpreted in cross section in Figures 8b and 12, have the correct orientations to produce some such discontinuities, but other reflections cross cut the inferred fault orientations. For the second possibility, northwest-striking fissures, many with lateral offsets, opened during the earthquake due to shaking and downslope movement, tectonic deformation, or both (see summary in McLaughlin and Clark, 2004). However, the imaged steep reflections extend well below topography and could not have been driven by downslope movement.

SAF reflectivity. The SAF itself does not appear to be reflective, although there are a number of weak reflections in the



vicinity of the interpreted fault, including the B reflections (Fig. 12). In contrast, in the Coachella Valley, the SAF is in one location reflective (see Fuis *et al.*, 2017, their fig. 6, southern Coachella Valley). However, where the SAF splits into the Banning and Mission Creek branches to the north of this location, only the Banning branch is reflective (see Fuis *et al.*, 2017, their Fig. 10, northern Coachella Valley).

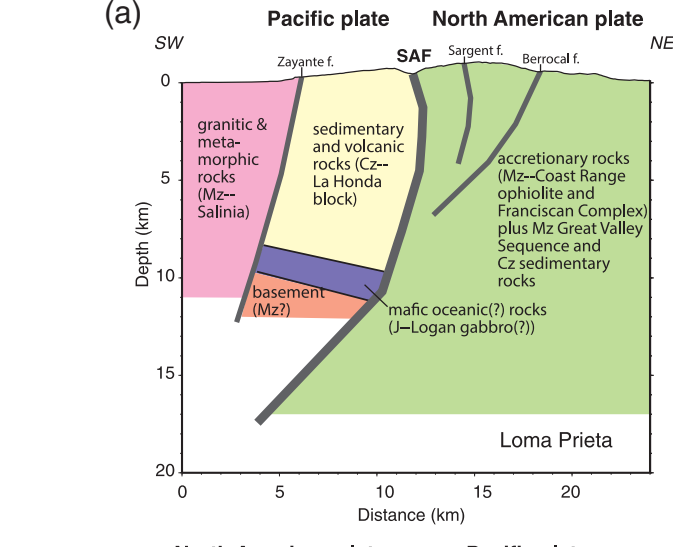
Reflectivity arises from velocity and density contrasts, which are in general present along most faults, owing the juxtaposition of different rock types. However, more importantly, fault zones can host low-velocity breccia, gouge, and fluid that differ significantly in velocity and density from that of the host rocks on either side. See the synthetic example in Figure A1, in which a narrow fault zone (white line) is embedded in a velocity model generating a high-amplitude reflection. Velocity contrasts between fault-zone rocks and host rocks can exceed 2 km/s (e.g., Ryberg and Fuis, 1998), whereas contrasts between different kinds of sedimentary, igneous, and metamorphic rocks that might be juxtaposed along a fault are generally much smaller (e.g., Clark, 1966). Having stated these facts, we have no clear interpretation for the lack of SAF reflectivity at Loma Prieta. SAF reflectivity appears variable in California and is a worthy subject for future investigation.

Near-surface northeast dip of SAF. The slight northeast dip of the SAF near the surface at Loma Prieta is surprising, although this dip is not as well constrained as the more prominent northeast dip along the profile 5 km to the southeast, where it was modeled by Jachens and Griscom (2004) as a block of magnetic Purisima Formation (sandstone) that extends in the subsurface northeast of the trace of the SAF

Figure 13. Seismotectonic summary of vicinity of 1989 $M_{\rm w}$ 6.9 Loma Prieta earthquake. (a) Rupture. Midcrustal slip summary taken from Beroza (1996). Mainshock focal mechanism from NCSN plotted at 3D relocation. Upper crustal displacement summary based on data in McLaughlin and Clark (2004). (b) Postrupture stress summary inferred from aftershock focal mechanisms (see Fig. 4c). P and T axes are schematic from approximate averages of majority of mechanisms.

(Fig. 7). In both the places, landslide material covering a buried zone of vertical fault splays might be an alternative interpretation. However, when steep strike-slip faults approach the surface in regions of topography, they are in some locations curved away from the higher topography; the actual fault is bent. See, for example, Sharp (1967, his fig. 3) for the San Jacinto fault. Similar bending is seen on the Banning fault in San Gorgonio pass, southern California (G. S. Fuis, author, mapping in 1972; Yule and Sieh, 2003, their fig. 9; J. C. Matti, written comm., 2020).

Focal mechanisms. Above 6 km depth, focal mechanisms for aftershocks (Fig. 4c) are chiefly reverse with lesser strike-slip motions, although the largest aftershock is strike slip and may have occurred on the Sargent fault. Below 10 km depth, there is a mix of chiefly normal and strike-slip mechanisms. For the reverse mechanisms located above 6 km depth and from the SAF to the northeast, the compression (P) direction is approximately horizontal and northeast–southwest, in the plane of the cross section, the same as documented in a prior study by Zoback *et al.* (1999) for this section of the SAF (in the southern part of the San Francisco peninsula). A similar pattern of stress and deformation is observed along



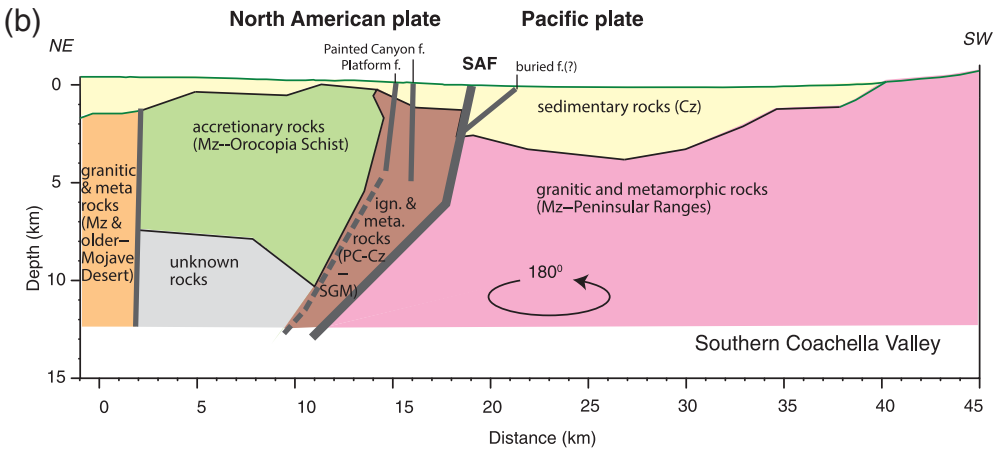


Figure 14. Comparison of SAF zones at Loma Prieta and in southern Coachella Valley. (a) Geologic and structural summary for Loma Prieta from this study. (b) Geologic and structural summary for southern Coachella Valley from Fuis *et al.* (2017, their fig. 6), rotated by 180°. SGM, Precambrian through Cenozoic igneous and metamorphic rocks of San Gabriel Mountains affinity. SAF is nonvertical and nonplanar in both the locations. Secondary, flower-structure-type faults, including Sargent and Berrocal faults at Loma Prieta and Painted Canyon and Platform faults in southern Coachella Valley are located in footwall at Loma Prieta but in hanging wall in southern Coachella Valley. These faults occur in older, chiefly accretionary rocks at both the locations and on North American plate. Cz, cenozoic; ign, igneous; meta, metamorphic; Mz, mesozoic; PC, precambrian.

the SAF throughout much of California (Mount and Suppe, 1987; Zoback et al., 1987). However, the pattern of fault normal compression at Loma Prieta is probably enhanced by the strike of the SAF here deviating 10°–12° counterclockwise from plate motion direction (see discussion in Zoback et al., 1999). A summary of seismotectonics at Loma Prieta (rupture and postrupture stress inferred from aftershocks) is shown in Figure 13. One possible interpretation of this summary is that the upper part of the hanging wall of the SAF moves as a blunt indentor or wedge into the upper part of the footwall, leading to the interpreted curved upper parts of the SAF and Sargent fault. As the hanging wall moves upward, the upper part of the hanging wall and footwall would be under

compression and the lower part of the hanging wall and footwall under extension, as reflected in the focal mechanisms.

A couple points of note here are the following: (1) The footwall in this (oblique slip) earthquake did actually move relatively downward, inspite of the fact that it contains Loma Prieta-the high point on our profile (Marshall and Stein, 1996). (2) Most of the aftershock mechanisms that align along our interpreted SAF and Sargent fault are actually reverse not strike slip (Fig. 4c), perhaps because compressional deformation is focused within the presumed damage zones of those faults.

Fault identity. One important conclusion to be drawn about our interpreted fault along the northeast side of the La Honda block is that it is a major fault. It offsets the two halves of the La Honda block: the one imaged beneath our profile at Loma Prieta and the one observed in the southern San Joaquin Valley. It is hard to escape the conclusion that this fault is not a secondary fault but is in fact the SAF itself.

Shaking hazard. The Earth's surface above the dipping segment of a fault (above the hanging wall) is closer to the rupture and gets shaken harder than the Earth's surface at equal distances on the opposite side of the fault (see, e.g., Boore *et al.*, 2014). This increased shaking was observed in 1989 in Santa Cruz (see Fig. 1 for location) compared to locations on the northeast side of the SAF (see Plafker and Galloway, 1990). Fuis *et al.* (2017) calculated that for a planar approximation to the dipping SAF in the Coachella Valley shaking is increased locally by up to a factor of 2 on the hanging wall and is decreased locally by up to a factor of 2 on the footwall, compared to shaking calculated for a vertical fault. Calculations have not yet been done for a nonplanar dipping fault, as interpreted in both the

Coachella Valley and at Loma Prieta. Observations are that peak ground acceleration was approximately doubled on the hanging walls compared to the footwalls for both the 1986 $M_{\rm w}$ 6.1 North Palm Springs earthquake, on the SAF in the Coachella Valley, and the 1989 $M_{\rm w}$ 6.9 Loma Prieta earthquake (see Fuis et al., 2012).

Summary of geology and geophysics

In summary, relocated earthquakes and velocity and aeromagnetic model boundaries are all consistent with an SAF that extends steeply downward from the surface in the upper few kilometers, perhaps with a slight initial northeast dip, and curves to join a moderately southwest-dipping mainshock rupture, itself nonplanar, below 6 km depth. This model requires no secondary fault as a source for the Loma Prieta earthquake. Thus, we interpret the 1989 Loma Prieta earthquake to have occurred solely on the SAF.

Comparison of SAF in Coachella Valley and at Loma **Prieta**

A motivation for this study was the model of the SAF in the Coachella Valley, which is interpreted to be nonvertical and nonplanar (Fuis et al., 2017). We compare the SAF structure in the Coachella Valley with that at Loma Prieta (Fig. 14), rotating the Coachella Valley structure 180° about a vertical axis for easier comparison. From these diagrams one would interpret that the SAF is indeed nonvertical and nonplanar in both the locations. A difference between these two locations is that active secondary (or flower-structure-like) faults in the Coachella Valley (Platform and Painted Canyon faults) are in the hanging wall of the SAF, whereas they are in the footwall (Sargent and Berrocal faults) at Loma Prieta. In both the cases, however, the secondary faults are in the older, chiefly accretionary rocks on the North American side of the SAF.

Loma Prieta and Coachella Valley are not the only locations where the SAF is nonvertical (Fuis et al., 2012; Fuis, 2019). In addition, in at least three places where there is detailed imaging (two locations in the Coachella Valley and one at Loma Prieta, in this study), the SAF is also nonplanar. The only place where the SAF is observed to be vertical and planar is in the western Mojave Desert (Fuis et al., 2003).

CONCLUSIONS

We interpret the SAF to be nonvertical and nonplanar at Loma Prieta, just as we interpret it to be in the Coachella Valley. Although the SAF apparently dips in opposite directions at Loma Prieta and in the Coachella Valley, it is associated with secondary faults on the same (North American) side in both the places, whereby secondary faults offset older, chiefly accretionary rocks.

For the following three chief reasons, we conclude that the 1989 $M_{\rm w}$ 6.9 Loma Prieta earthquake occurred on the SAF and not on a secondary fault within the SAF zone: (1) The Loma Prieta rupture occurred on a fault interpreted in this study to extend upward to the surface trace of the SAF. There is little evidence for a vertical or planar fault below 10 km depth beneath the trace of the SAF, and no secondary fault is required as the earthquake source. (2) The interpreted fault forms the northeast side of the La Honda block, and this fault could only be a major plate-bounding fault to offset the La Honda block from its other half in the southern San Joaquin Valley. This offset could not have been accomplished by a secondary fault, and (3) this interpreted fault is consistent in geometry with the SAF imaged in the Coachella Valley. Its nonvertical, nonplanar geometry is not unique to Loma Prieta.

DATA AND RESOURCES

The aeromagnetic data set reported in Abrams et al. (1991) is available at https://pubs.er.usgs.gov/publication/ofr9130. The Northern California Seismic Network (NCSN) earthquake catalog is available at https:// www.ncedc.org/ncedc/catalog-search.html. The U.S. Geological Survey (USGS) Open-File Report of Oppenheimer et al. (1993) is available at https://pubs.usgs.gov/of/1993/0578/report.pdf. The USGS Open-File Report of Reasenberg and Openheimer (1985) is available at https:// pubs.er.usgs.gov/publication/ofr85739. The catalog of Waldhauser and Schaff (2008) is available at https://www.ldeo.columbia.edu/~felixw/ NCAeqDD/. The USGS Open-File Report of Zhang et al. (2018) is available at doi: 10.3133/ofr20181093. All the websites were last accessed in February 2022. The supplemental material cites potential field modeling software and presents three prior models of aeromagnetic and gravity data.

DECLARATION OF COMPETING INTERESTS

The authors acknowledge that there are no conflicts of interest recorded.

ACKNOWLEDGMENTS

The authors appreciate reviews of earlier drafts of this article by Tom Brocher, Pat McCrory, Cliff Thurber, and five anonymous reviewers at BSSA. Discussions with colleagues at the U.S. Geological Survey (USGS), including Wayne Thatcher, Bob McLaughlin, and Rick Stanley, who improved this article.

REFERENCES

Abrams, G. A., R. P. Kucks, and R. E. Bracken (1991). Aeromagnetic gridded data for a portion of the San Jose 1 degree x 2 degrees Quadrangle, California, U.S. Geol. Surv. Open-File Rept. 91-30, 4 pp. Aydin, A., and B. M. Page (1984). Diverse Pliocene-Quaternary tec-

tonics in a transform environment, San Francisco Bay region, California, GSA Bull. 95, 1303-1317.

Bauer, K., T. Ryberg, G. S. Fuis, and S. Lueth (2013). Seismic imaging of the Waltham Canyon fault, California: Comparison of ray-theoretical and Fresnel volume prestack depth migration, Bull. Seismol. Soc. Am. 103, 340-352.

Beroza, G. C. (1991). Near-source modeling of the Loma Prieta earthquake: Evidence for heterogeneous slip and implications for earthquake hazards, Bull. Seismol. Soc. Am. 81, 1603-1621.

- Beroza, G. C. (1996). Rupture history of the earthquake from high-frequency strong-motion data, *U.S. Geol. Surv. Profess. Pap. 1550-A*, 9–32.
- Boore, D. M., J. P. Stewart, E. Seyhan, and G. M. Atkinson (2014). NGA-West2 equations for predicting PGA, PGV, and 5% damped PSA for shallow crustal earthquakes, *Earthq. Spectra* **30**, 1057–1085.
- Brocher, T. M., M. J. Moses, and S. D. Lewis (1992). Wide-angle seismic recordings obtained during seismic reflection profiling by the S.P. Lee offshore the Loma Prieta epicenter, U.S. Geological Survey Open File Report 92-245, 63.
- Bürgmann, R., R. Arrowsmith, T. Dumitru, and R. McLaughlin (1994). Rise and fall of the southern Santa Cruz mountains, California, from fission tracks, geomorphology, and geodesy, *J. Geophys. Res.* **99**, 20,181–20,202.
- Catchings, R. D., M. R. Goldman, C. E. Steedman, and G. Gandhok (2004). Velocity models, first-arrival travel times, and geometries of 1991 and 1993 USGS land-based controlled-source seismic investigations in the San Francisco Bay area, California—In-line shots, U.S. Geol. Surv. Open-File Rept. 2004-1423, 32 pp.
- Clark, J. C. (1981). Stratigraphy, paleontology, and geology of the central Santa Cruz Mountains, California Coast Ranges, U.S. Geol. Surv. Profess. Pap. 1168, 51 pp.
- Clark, S. P., Jr. (1966). Handbook of Physical Constants, Vol. 97, Geological Society of America Memoir, Boulder, Colorado, 587 pp.
- Cummings, J. C., R. M. Touring, and E. E. Brabb (1962). Geology of the northern Santa Cruz Mountains, California, Geologic guide to the gas and oil fields of northern California, in *California Division of Mines and Geology Bulletin 181*, O. E. Bowen Jr. (Editor), 179–220.
- Dietz, L. D., and W. L. Ellsworth (1990). The October 17, 1989, Loma Prieta, California, earthquake and its aftershocks: Geometry of the sequence from high-resolution locations, *Geophys. Res. Lett.* 17, 1417–1420.
- Dietz, L. D., and W. L. Ellsworth (1997). Aftershocks of the Loma Prieta earthquake and their tectonic implications, U.S. Geol. Surv. Profess. Pap. 1550-D, 5-47.
- Eaton, J. P. (1990). The earthquake and its aftershocks from May 2 through September 30, *U.S. Geol. Surv. Profess. Pap. 1487*, 113–170.
- Eberhart-Phillips, D. (1991). The 1991 active seismic experiment in the Loma Prieta, California region: Shallow seismicity and fault structure, *Eos Trans. AGU* **72**, 311.
- Eberhart-Phillips, D., and A. J. Michael (1998). Seismotectonics of the Loma Prieta, California, region determined from three-dimensional Vp, Vp/Vs, and seismicity, *J. Geophys. Res.* **103**, 21,099–21,120.
- Eberhart-Phillips, D., and A. J. Michael (2004). Seismotectonics of the Loma Prieta region determined from three-dimensional P-wave velocities, Vp/Vs ratios, and seismicity, U.S. Geol. Surv. Profess. Pap. 1550-E, 165–188.
- Feld, C., J. Mechie, C. Hübscher, J. Hall, S. Nicolaides, C. Gurbuz, K. Bauer, K. Louden, and M. Weber (2017). Crustal structure of the Eratosthenes Seamount, Cyprus and S. Turkey from an amphibian wide-angle seismic profile, *Tectonophysics* 700/701, 32–59, doi: 10.1016/j.tecto.2017.02.003.
- Foxall, W., A. Michelini, and T. V. McEvilly (1993). Earthquake travel time tomography of the southern Santa Cruz Mountains: Control

- of fault rupture by lithological heterogeneity of the San Andreas fault zone, *J. Geophys. Res.* **98**, 17,691–17,710, doi: 10.1029/93JB01424.
- Fuis, G. S. (2019). Subsurface geometry of the San Andreas fault in southern and central California, 2019 Fall Meeting, AGU, San Francisco, California, 10–14 December, Abstract S23G-0719.
- Fuis, G. S., K. Bauer, M. R. Goldman, T. Ryberg, V. E. Langenheim, D. S. Scheirer, M. J. Rymer, J. M. Stock, J. A. Hole, R. D. Catchings, et al. (2017). Subsurface geometry of the San Andreas fault in southern California: Results from the Salton Seismic Imaging Project (SSIP) and strong ground motion expectations, Bull. Seismol. Soc. Am. 107, 1642–1662, doi: 10.1785/0120160309.
- Fuis, G. S., R. W. Clayton, P. M. Davis, T. Ryberg, W. J. Lutter, D. A. Okaya, E. Hauksson, C. Prodehl, J. M. Murphy, M. L. Benthien, et al. (2003).
 Fault systems of the 1971 San Fernando and 1994 Northridge earthquakes, southern California: Relocated aftershocks and seismic images from LARSE II, Geology 31, 171–174.
- Fuis, G. S., T. Ryberg, N. J. Godfrey, D. A. Okaya, and J. M. Murphy (2001). Crustal structure and tectonics from the Los Angeles basin to the Mojave Desert, southern California, *Geology* 29, 15–18.
- Fuis, G. S., D. S. Scheirer, V. E. Langenheim, and M. D. Kohler (2012).
 A new perspective on the geometry of the San Andreas Fault in southern California and its relationship to lithospheric structure,
 Bull. Seismol. Soc. Am. 102, doi: 10.1785/0120110041.
- Gardner, G. H. F., L. W. Gardner, and A. R. Gregory (1974). Formation velocity and density—The diagnostic basics for stratigraphic traps, *Geophysics* 39, 770–780.
- Gooley, J. T., G. R. Sharman, and S. A. Graham (2020). Reconciling along-strike disparity in slip displacement of the San Andreas fault, central California, USA, GSA Bull. 133, 1441–1464.
- Hauksson, E., and P. Shearer (2005). Southern California hypocenter relocation with waveform cross-correlation: Part 1, Results using the double-difference method, *Bull. Seismol. Soc. Am.* 95, 896–903, doi: 10.1785/0120040167.
- Hauksson, E., W. Yang, and P. M. Shearer (2012). Waveform relocated earthquake catalog for southern California (1981 to June 2011), *Bull. Seismol. Soc. Am.* **102**, 2239–2244, doi: 10.1785/0120120010.
- Hole, J. (1992). Nonlinear high-resolution three-dimensional seismic travel time tomography, *J. Geophys. Res.* **97**, 6553–6562.
- Jachens, R. C., and A. Griscom (2004). Geophysical and geologic setting of the earthquake, inferred from gravity and magnetic anomalies, U.S. Geol. Surv. Profess. Pap. 1550-E, 49–80.
- James, E. W., D. L. Kimbrough, and J. M. Mattinson (1994).
 Evaluation of displacements of pre-Tertiary rocks on the northern
 San Andreas fault using U-Pb zircon dating, initial Sr, and
 common Pb isotopic ratios, in Chap. 7 of The San Andreas
 Fault System; Displacement, Palinspastic Reconstruction, and
 Geologic Evolution, R. E. Powell, R. J. Welldon, and J. C. Matti
 (Editors), Vol. 178, Geological Society of America Memoir,
 Boulder, Colorado, 257–271.
- Jennings, C. W., and W. A. Bryant (2010). Fault activity map of California, California Geol. Surv. Geologic Data Map No. 6, map scale 1:750,000.
- Lin, G., and P. Shearer (2005). Tests of relative earthquake location techniques using synthetic data, *J. Geophys. Res.* **110**, no. B4, doi: 10.1029/2004JB003380.

- Lin, G., and C. H. Thurber (2012). Seismic velocity variations along the rupture zone of the 1989 Loma Prieta earthquake, California, *Bull. Seismol. Soc. Am.* 117, no. B9, doi: 10.1029/2011JB009122.
- Lin, G., P. M. Shearer, and E. Hauksson (2007). Applying a three-dimensional velocity model, waveform cross correlation, and cluster analysis to locate southern California seismicity from 1981 to 2005, *J. Geophys. Res.* 112, no. B12, doi: 10.1029/2007JB004986.
- Lin, G., P. M. Shearer, E. Hauksson, and C. H. Thurber (2007). A three dimensional crustal seismic velocity model for southern California from a composite event method, *J. Geophys. Res.* 112, no. B11, doi: 10.1029/2007[B004977.
- Marshall, G. A., and R. S. Stein (1996). Elevation changes associated with the earthquake and their use to infer fault-slip geometry, *U.S. Geological Survey Professional Paper 1550-A*, 105–146.
- Mavko, G., T. Mukerji, and J. Dvorkin (1998). *The Rock Physics Handbook*, University Printing House, Cambridge University Press, Cambridge, United Kingdom, 329 pp.
- McLaughlin, R. J. (1974). The Sargent-Berrocal fault zone and its relation to the San Andreas fault system in the southern San Francisco Bay region and Santa Clara Valley, *J. Res. U.S. Geol. Surv.* **2,** 593–598.
- McLaughlin, R. J., and J. C. Clark (2004). Stratigraphy and structure across the San Andreas fault zone in the Loma Prieta region and deformation during the earthquake, *U.S. Geol. Surv. Profess. Pap.* 1550–E, 5–48.
- McLaughlin, R. J., and A. Griscom (2004). Maps showing residual-magnetic fields, isostatic-residual-gravity fields, and generalized geology of the southern San Francisco Bay and Loma Prieta regions, California, U.S. Geol. Surv. Profess. Pap. 1550-E, pl. 3.
- McLaughlin, R. J., J. C. Clark, E. E. Brabb, E. J. Helley, and C. M. Wentworth (2004). Geologic map of the Loma Prieta region, California, U.S. Geol. Surv. Profess. Pap. 1550–E, pl. 1.
- Mount, V. S., and J. Suppe (1987). State of stress near the San Andreas fault: Implications for wrench tectonics, *Geology* **15**, 1142–1146.
- Oppenheimer, D. H., F. W. Klein, J. P. Eaton, and F. W. Lester (1993). The Northern California Seismic Network bulletin, January–December 1992, U.S. Geol. Surv. Open-File Rept. 93-578, doi: 10.3133/ofr93578.
- Plafker, G., and J. P. Galloway (1990). Lessons learned from the Loma Prieta, California, Earthquake of October 17, 1989, *U.S. Geological* Survey Circular 1045, 48.
- Reasonberg, P. A., and D. H. Oppenheimer (1985). FPFIT, FPPLOT and FPPAGE; Fortran computer programs for calculating and displaying earthquake fault-plane solutions, *U.S. Geol. Surv. Open-File Rept.* 85-739, doi: 10.3133/ofr85739.
- Richards-Dinger, K. B., and P. M. Shearer (2000). Earthquake locations in southern California obtained using source-specific station terms, *J. Geophys. Res.* **105**, 10,939–10,960.
- Ross, D. C. (1970). Quartz gabbro and anorthositic gabbro: Markers of offset along San Andreas fault in California Coast Ranges, GSA Bull. 81, 3647–3662.
- Ross, D. C. (1978). The Salinian block—a Mesozoic granitic orphan in the California Coast Ranges, in *Mesozoic paleogeography of the western United States (Pacific Coast Paleogeography Symposium 2)*, D. G. Howell and K. A. McDougall (Editors), Society of

- Economic Paleontologists and Mineralogists, Pacific Section, Los Angeles, California, 509–522.
- Ryberg, T., and G. S. Fuis (1998). The San Gabriel Mountains bright reflective zone: Possible evidence of young mid-crustal thrust faulting in southern California, *Tectonophysics* **286**, 31–46.
- Ryberg, T., C. Haberland, T. Haberlau, M. H. Weber, K. Bauer, J. H. Behrmann, and W. Jokat (2015). Crustal structure of northwest Namibia: Evidence for plume-rift-continent interaction, *Geology* **43**, 739–742, doi: 10.1130/G36768.1.
- Schaff, D. P., and F. Waldhauser (2005). Waveform cross-correlation-based differential travel-time measurements at the Northern California Seismic Network, *Bull. Seismol. Soc. Am.* 95, 2446–2461.
- Sharp, R. V. (1967). San Jacinto fault zone in the Peninsular Ranges of southern California, *Geol. Soc. Am. Bull.* **78**, 705–730.
- Spudich, P., and J. Orcutt (1980). A new look at the seismic velocity structure of oceanic crust, *Rev. Geophys.* 18, 627–645.
- Stanley, R. G. (1985). Middle Tertiary sedimentation and tectonics of the La Honda basin, central California, *U.S. Geological Survey Open-File Report 85-596*, 263.
- Thurber, C. H., T. M. Brocher, H. Zhang, and V. E. Langenheim (2007). Three-dimensional P wave velocity model for the San Francisco Bay region, California, *J. Geophys. Res.* **112**, no. B7, doi: 10.1029/2006JB004682.
- Tsutsumi, H., and R. S. Yeats (1999). Tectonic setting of the 1971 Sylmar and 1994 Northridge earthquakes in the San Fernando Valley, California, *Bull. Seismol. Soc. Am.* **89**, 1232–1249.
- Wald, D. J., D. V. Helmberger, and T. H. Heaton (1991). Rupture model of the 1989 Loma Prieta earthquake from the inversion of strong-motion and broadband teleseismic data, *Bull. Seismol. Soc. Am.* 81, 1540–1572.
- Waldhauser, F., and W. L. Ellsworth (2000). A double-difference earthquake location algorithm: Method and application to the northern Hayward fault, California, Bull. Seismol. Soc. Am. 90, 1353–1368.
- Waldhauser, F., and D. P. Schaff (2008). Large-scale relocation of two decades of Northern California seismicity using cross-correlation and double-difference methods, *J. Geophys. Res.* 113, no. B8, doi: 10.1029/2007JB005479.
- Yilmaz, O. (1987). Seismic Data Processing, Society Exploration Geophysicists, Tulsa, Oklahoma, 526 pp.
- Yule, D., and K. Sieh (2003). Complexities of the San Andreas fault near San Gorgonio Pass: Implications for large earthquakes, *J. Geophys. Res.* **108**, doi: 10.1029/2001JB000451.
- Zhang, E., G. S. Fuis, R. D. Catchings, D. S. Scheirer, M. Goldman, and K. Bauer (2018). Reexamination of the subsurface fault structure in the vicinity of the 1989 moment-magnitude-6.9 Loma Prieta earthquake, central California, using steep-reflection, earthquake, and magnetic data, U.S. Geol. Surv. Open-File Rept. 2018-1093, 35 pp.
- Zoback, M. D., M. L. Zoback, V. S. Mount, J. Suppe, J. P. Eaton, J. H. Healy, D. Oppenheimer, P. Reasenberg, L. Jones, C. B. Raleigh, et al. (1987). New evidence on the state of stress of the San Andreas fault system, Science 238, 1105–1111.
- Zoback, M. L., R. C. Jachens, and J. A. Olsen (1999). Abrupt alongstrike change in tectonic style: San Andreas Fault zone, San Francisco peninsula, *J. Geophys. Res.* **104**, 10,719–10,742.

APPENDIX Reflection analysis

Reflection analysis consisted of automatic detection of coherent secondary arrivals in individual record sections followed by prestack depth migration of these detected phases (Bauer et al., 2013). Preprocessing of the seismic reflection data included dead trace removal, non-zero mean of amplitudes in a seismic trace (DC) removal, top muting, band-pass filtering (2–16 Hz), spectral whitening, automatic gain control (2 s operator length), and deconvolution (80 ms operator length). The work flow applied after the preprocessing is illustrated by synthetic example Figure A1: (a) Shot gathered data are analyzed in the time domain using a moving window. Only windowed samples are considered. (b) A point i is chosen at the center of this window in which a semblance (coherence) analysis is carried out. Local slant stacks over neighboring traces are calculated for a given range of slowness values. The local slant stack with the highest coherence value defines the local slowness of the wave field at the analyzed sample i. For coherence exceeding 0.5 and absolute value of normalized amplitude exceeding 0.1, a line segment is drawn in the time

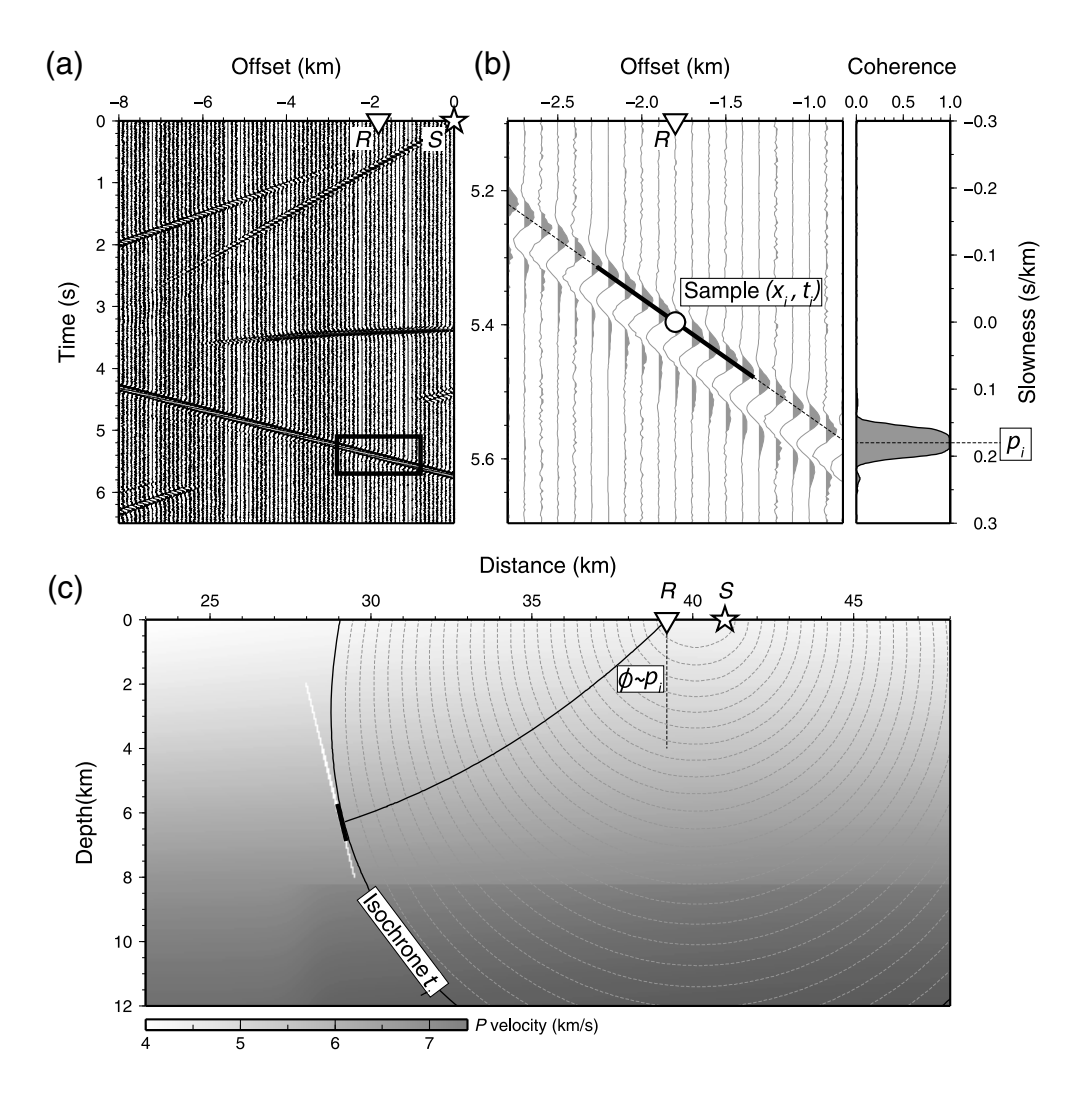


Figure A1. (a) Synthetic data illustrating prestack line migration method of Bauer *et al.* (2013). R, receiver; S, shot point. Black rectangle is a moving window in which the maximum semblance (coherence) is calculated. (b) Enlargement of moving window of (a) in which coherence analysis is carried out. Small circle is point of calculation centered at offset x_i and time t_i for receiver R. Line segment (bold black line) corresponds to slowness p_i with the maximum coherence for this window. Minimum coherence of 0.5 and minimum absolute value of normalized amplitude of 0.1 is required for a detection. (c) Prestack migration to map line segment from time to depth domain. Ray tracing starts at receiver R. Initial ray direction Φ is defined by given velocity at receiver and slowness p_i derived from coherence analysis. Migration point is determined where ray crosses isochrone for reflection time t_i . Note that white line tangent to isochrone t_i is geologic contact or low-velocity fault zone causing reflection. V.E. 1:1, vertical exaggeration.

domain with the corresponding dip and centered at the analyzed sample. (c) A prestack migration is then used to map the line segment from the time domain into the depth domain based on a given velocity model. A ray is shot from the receiver downward. The initial angle of the ray is defined by the given velocity at the receiver and the slowness p_i derived from the coherence analysis. The line is migrated to the location where the ray crosses the isochrone. The isochrone represents subsurface locations of equal reflection time t_i for a given coherent

sample *i*. Finally, the line segment is drawn at the migration point with the local dip in the depth domain. More details on the prestack line migration are described in Bauer *et al.* (2013). Applications of the method and more practical aspects can be found in Ryberg *et al.* (2015), Feld *et al.* (2017), and Fuis *et al.* (2017).

Manuscript received 17 March 2022 Published online 6 September 2022